

---

Wesleyan University

---

**The Debris Disk Around AU Mic:  
Measuring the Scale Height as a Proxy  
for Probing the Strengths of Bodies in  
the Collisional Cascade**

by

Evan Carter

Faculty Advisor: A. Meredith Hughes

A thesis submitted to the  
faculty of Wesleyan University  
in partial fulfillment of the requirements for the  
Degree of Master of Arts in Astronomy

---

Middletown, Connecticut

---

---

May, 2018

---

# Table of Contents

<b>1</b>	<b>Introduction</b>	<b>1</b>
1.1	Evolution of Circumstellar Disks . . . . .	2
1.2	Observations of Debris Disks . . . . .	6
1.3	Physics of the Collisional Cascade . . . . .	9
1.4	AU Microscopii . . . . .	11
<b>2</b>	<b>Observations</b>	<b>16</b>
<b>3</b>	<b>Analysis</b>	<b>22</b>
3.1	Modeling the Debris Disk Around AU Mic . . . . .	23
3.2	Results: Resolved Scale Height . . . . .	29
3.3	Dust Grain Size Distribution: $q$ . . . . .	31
3.4	Velocity Dispersion in the Disk: $p$ . . . . .	34
<b>4</b>	<b>Discussion</b>	<b>36</b>
4.1	AU Mic Debris Disk Characteristics . . . . .	37
4.2	Constraints on the Collisional Cascade: $q$ and $p$ . . . . .	41
<b>5</b>	<b>Conclusion</b>	<b>45</b>
	<b>Bibliography</b>	<b>48</b>

# Chapter 1

## Introduction

The dusty, tenuous debris disks that encircle up to 20 – 25% of main sequence stars represent the final phase of a fully matured planetary system (Eiroa et al. 2013; Montesinos et al. 2016; Hughes et al. 2018). Such disks are widely believed to be hallmarks of significant reservoirs of planetesimals, as the dust that we observe in the disk is thought to be produced via the grinding down of larger bodies during collisions, a concept referred to as the collisional cascade (Dohnanyi 1969). In this model, dynamical “stirring” by the largest bodies in the disk can gravitationally perturb the orbits of smaller grains, inducing inclinations to their orbits that push them out of the disk midplane. This gravitational “puffing up” of the debris disk height therefore encodes unique information about the system dynamics (Wetherill & Stewart 1993; Artymowicz 1997; Quillen et al. 2007), including possible insight into the eventual formation of planets in the disk (Wyatt 2008). Observations capable of spatially resolving the vertical structure of debris disks can therefore reveal information essential to building a comprehensive theory of planet formation. In this chapter, we outline some of the fundamental aspects of debris disks, including their formation and evolution, observational character-

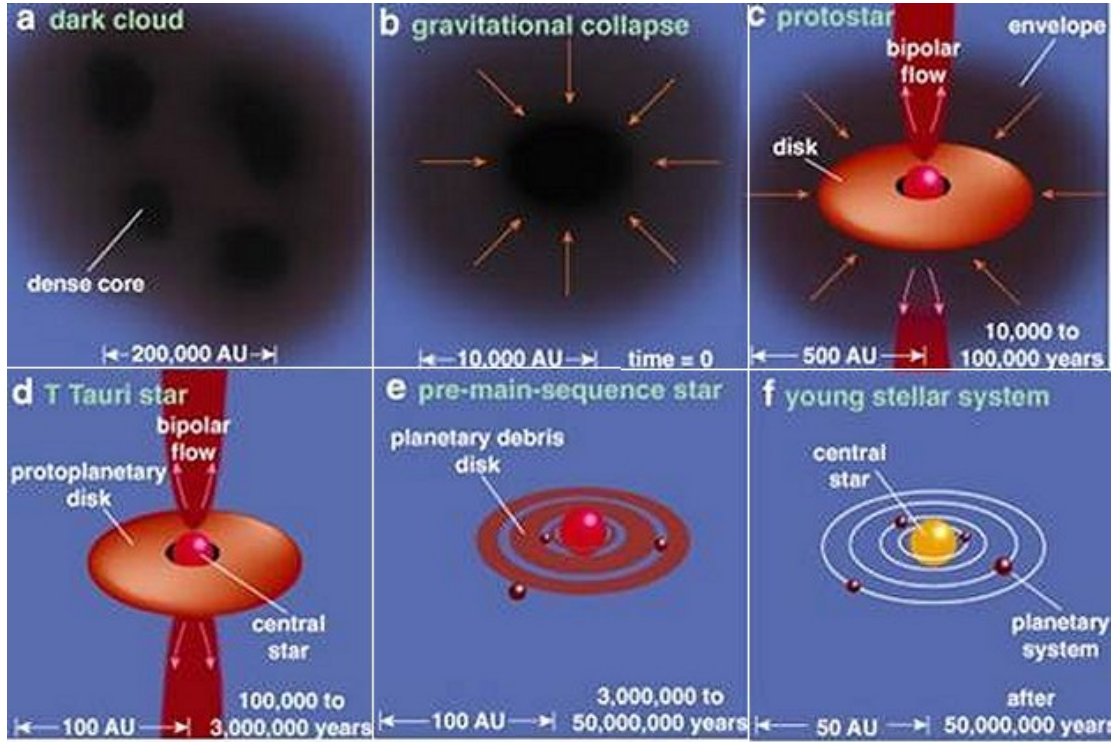


Figure 1.1: Overview of the formation of a star and accompanying circumstellar disk, from Greene (2001). (a) Fragmentation of overdense regions within a Giant Molecular Cloud. (b) Collapse due to gravitational instability of a pre-stellar core. (c) Formation of the accretion disk and core from the collapsing protostellar envelope. (d) Protostar with a bipolar flow driven by disk accretion, dissipation of the outer envelope. (e) Debris disk populated with large amounts of dust. (f) Fully mature stellar system, with the majority of dust locked up within the largest bodies present in the system.

istics, and a further discussion of the canonical collisional cascade model used to describe them. Finally, we describe recently obtained observations of the debris disk around AU Microscopii, an ideal candidate for observation due to its proximity and brightness at millimeter wavelengths.

## 1.1 Evolution of Circumstellar Disks

McKee & Ostriker (2007) refer to stars as the “atoms of the universe” based on their influence over everything from the structure and luminosity of galaxies, to

the production of many of the chemical elements via nuclear fusion in the stellar interior. The formation and evolution of a planetary system is likewise deeply intertwined with the formation of its parent star. Star formation begins within the cold, dense interior of a Giant Molecular Cloud (GMC) composed of primarily hydrogen gas with some helium and trace amounts of metals. Localized regions of increased density within the GMC arise due to the occurrence of a nearby supernova, interactions between neighboring clouds, or the passage of spiral arms, eventually becoming gravitationally unstable (Jeans 1929; Ebert 1955; Bonnor 1956; Elmegreen 2012). These regions then fragment and collapse inwards to form dense protostellar cores shrouded in an envelope of in-falling material (Hoyle 1953). Due to the large initial size of the cloud, small turbulence-driven rotations lead to a large amount of angular momentum, that must be conserved as the core contracts. In fact, the net angular momentum of the collapsing core is so large that unless it is somehow dissipated outwards the star will not be able to form. During contraction of the core, the protostellar envelope settles into a viscous circumstellar accretion disk (Lynden-Bell & Pringle 1974; Durisen et al. 1986; Krumholz 2011; Williams & Cieza 2011). The disk aids the formation of the nascent star by dissipating the angular momentum in two ways: by allowing the dissipation of angular momentum radially outwards through the disk, and by feeding material inwards onto the central star. The accretion from the disk launches a bipolar outflow that clears away a cavity in the envelope (Shu et al. 1987).

As the protostar continues to contract and accrete material from the disk, it eventually becomes hot and dense enough within the core to initiate hydrogen fusion. Eventually, any remaining material settles into the orbital plane of the system, leaving behind a protoplanetary disk (PPD) with a radial extent that

depends on both the rotation of the parent star and the timescale of in-falling material from the initial envelope (Terebey et al. 1984a). The PPD is optically thick at optical and infrared (OIR) wavelengths and gas rich, with a commonly assumed gas-to-dust ratio of as much as  $\sim 100 : 1$  by mass, based on constraints from the Interstellar Medium (ISM), which may or may not be justified (Bohlin et al. 1978; Tricco et al. 2017).

The majority of primordial gas and dust in the PPD will dissipate from the disk due to accretion onto the parent star, which clears out the innermost region of the disk (Dullemond & Monnier 2010; Williams & Cieza 2011), photoevaporation from stellar winds, which shapes the gravitational radius of the disk (Clarke et al. 2001), or accretion onto planetary embryos (Safronov & Zvjagina 1969). The clearing of primordial dust from the disk occurs on a timescale of roughly  $\sim 10$  Myr (Mamajek 2009). During this time, planetesimals begin to form out of the dust grains in the disk. A period of runaway growth is triggered when the planetesimal becomes sufficiently large ( $\sim 1$  km) such that gravitational forces dominate over viscous drag forces from the gas. These planetesimals generate a gravitational field large enough to perturb the orbits of other bodies, inducing collisions with increased probability and raising the rate of fragmentation or accretion onto the planetesimal (Chambers 2010). Shortly afterward, planetesimals undergo a period of oligarchic growth, in which the largest body within a region clears its orbit of smaller bodies and other material. Oligarchic growth continues until the protoplanet contains approximately  $1/2$  of the material by mass within the region, occurring over a timescale of up to a few Myr (Wetherill & Stewart 1993; Kokubo et al. 1998). Eventually the primordial disk material has all but completely dispersed, leaving behind a gas-poor disk largely populated by second-generation material (Hughes et al. 2018). Figure 1.1 traces the evolution of a circumstellar disk from the initial

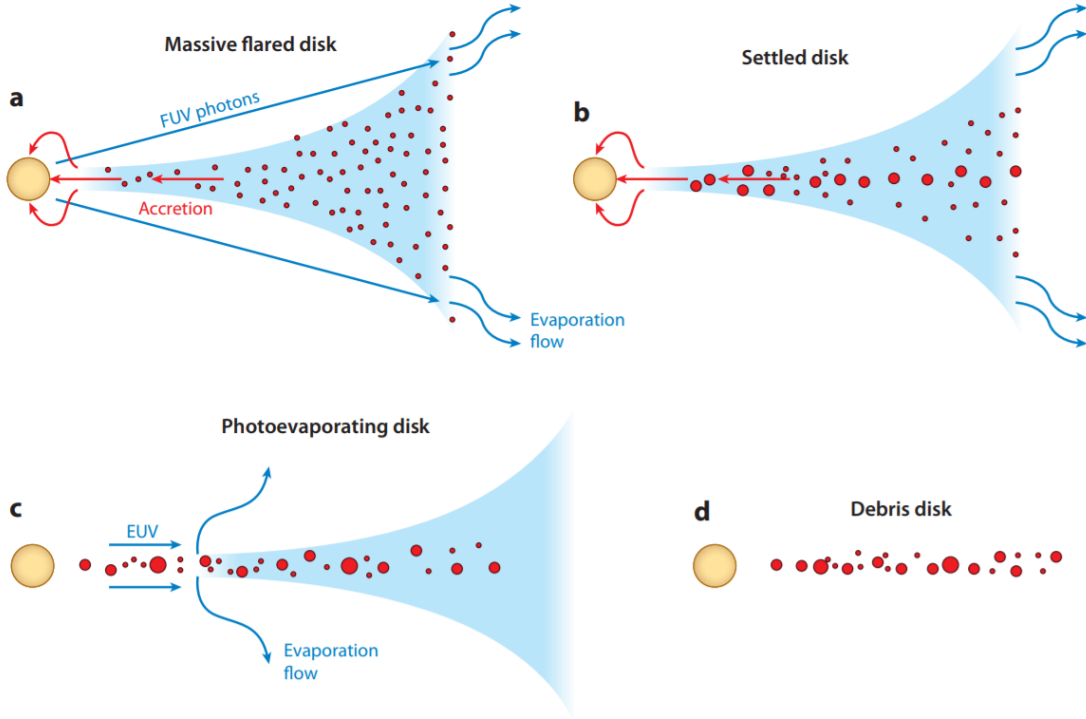


Figure 1.2: Diagram from Williams & Cieza (2011) illustrating the dissipation of primordial material from the circumstellar disk. (a) Disk mass loss due to photoevaporation from extreme ultraviolet (UV) light and accretion onto the parent star. (b) Grain growth into larger-size bodies and consequent gravitational settling onto the disk midplane (c) As disk mass and accretion rate decrease, photoevaporation eventually prevents the outer disk from replenishing the inner part of the disk. Accretion stops, and the disk dissipates from the inside out (d) Final stage of a circumstellar disk, after the primordial gas has been almost completely dispersed.

GMC collapse to a dusty, tenuous debris disk populated by second-generation material (Williams & Cieza 2011). A diagram showing the effects of accretion and photoevaporation driving the dissipation of disk material is shown in figure 1.2. In the next section, we discuss how observations of debris disks can allow us to gain insight on the dynamics of these systems.

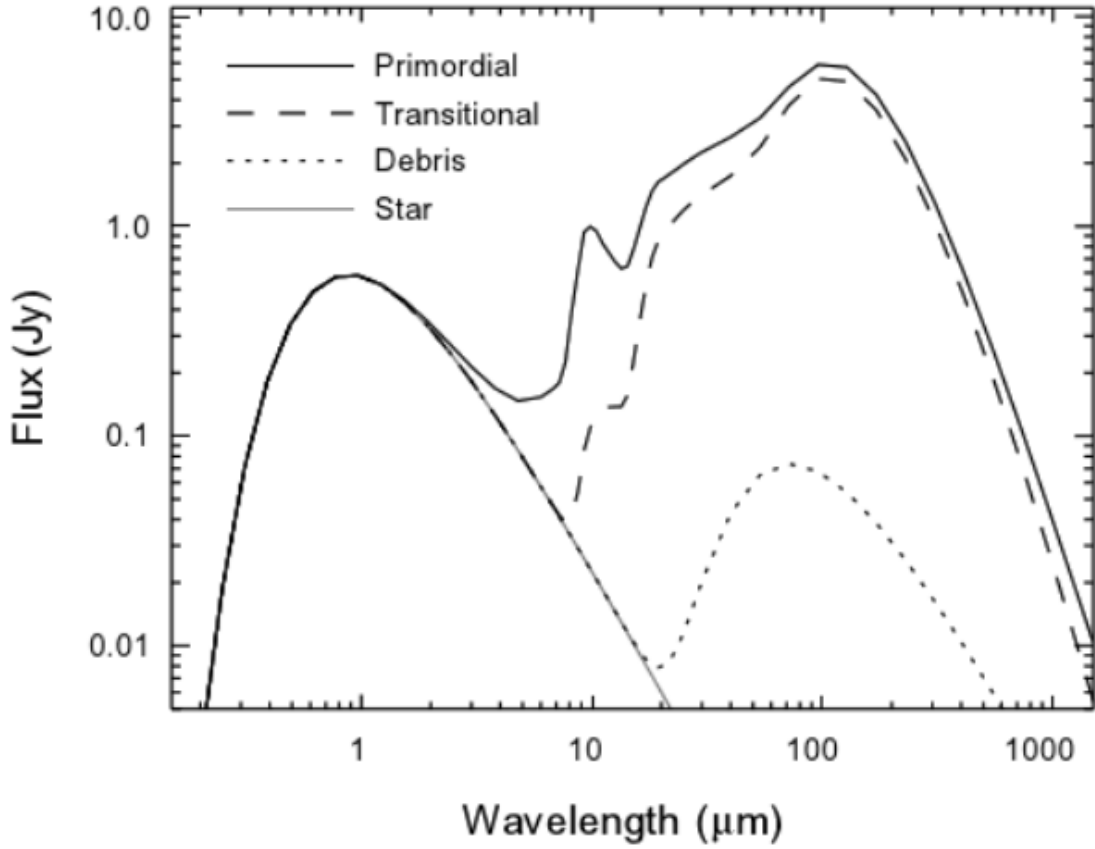


Figure 1.3: Theoretical spectra for each of the three main classes of circumstellar disks from Roberge & Kamp (2010). The protoplanetary and transition disk spectra were created using the CGPlus code (Dullemond et al. 2001), while the debris disk spectrum is modeled as a blackbody with  $T = 70$  K. Note the distinct secondary “hump” of excess emission at IR/millimeter wavelengths in the debris disk SED, due to thermal radiation from the dust grain population.

## 1.2 Observations of Debris Disks

The first debris disks was detected around the star Alpha Lyrae by Aumann et al. (1984) as an infrared (IR) excess above the expected results for the stellar photosphere using observations from the *Infrared Astronomical Satellite* (IRAS). This excess is due to blackbody radiation from dust grains within the disk, that exceeds stellar emission at millimeter wavelengths (see figure 1.3). While IR-



excesses are the typical method for detecting debris disks, observations of disks across the electromagnetic spectrum have been conducted (Hughes et al. 2018), due to the fact that collisions between planetesimals produce dust grains at a variety of sizes.

A common assumption regarding observations of dust, whether in scattered optical light or thermal radiation at longer wavelengths, is that the wavelength of observation is of order the size of the grain population under observation (Hughes et al. 2018). This correspondence is made possible by the interaction of two competing trends: the first is that dust grains are only efficient emitters of radiation at wavelengths shorter than their physical size. At wavelengths longer than the size of the grain, the emission efficiency drops sharply. The second is that the grain size distribution in the collisional cascade (see Equation 1.1) is heavily weighted towards smaller grains. While this bias towards small grains may seem to contradict the fact that much of the dust mass in the disk is contained within the largest bodies, the surface brightness of the disk is dominated by small grains due to their large surface area. These two factors result in the total light output being due to the smallest grains that can emit efficiently, which are of sizes approximately equal to the wavelength of observation.

Observations of debris disks across multiple wavelengths thus reveal a great detail of information concerning the distribution of dust populations at different grain sizes. In particular, observations at far-IR/millimeter wavelengths probe the largest grains that participate in dust production, which are correlated with the distribution of planetesimals within the disk that would otherwise be too faint to detect. This correlation stems from the fact that large grains are more weakly influenced by the non-gravitational forces that sculpt smaller grains in the disk, such as radiation pressure and stellar winds. The relative velocities of bodies

induced into collisions are similarly determined by processes relating to the largest bodies within the system, including dynamical stirring of smaller grains. This stirring introduces orbital inclinations that kick grains out above and below the midplane of the disk. The vertical structure of a debris disk thus encodes unique information into the dynamics dictated by the largest bodies in the disk, which we can directly relate to the physics involved in collisional cascade. The vertical scale height of the system, which characterizes the natural mass density distribution of dust above the disk midplane, is a particularly useful measurement as it directly encodes the velocity dispersion of dynamically stirred grains (Artymowicz 1997; Quillen et al. 2007; Thébault & Augereau 2007). We can therefore use observations of the scale height in debris disks, provided they are spatially resolved, in order to place constraints on the bodies involved in the collisional cascade model.

Previous efforts have been made to measure the scale height of debris disks at OIR wavelengths (Artymowicz 1997; Krist et al. 2005). However, theoretical work by Thébault (2009) showed that dust grains at sized probed by OIR wavelengths are susceptible to increased eccentricities and inclinations brought about by stellar radiation effects, leading to a “natural scale height” that will be observed in OIR observations, regardless of the presence of large stirring bodies. It is therefore important to conduct observations at far-infrared (FIR) and (sub)millimeter wavelengths, where the effects of stellar radiation on dust grain dynamics is dwarfed by the force of gravity. Currently, the Atacama Large Millimeter/submillimeter Array (ALMA) represents the best choice of instrument for attempting to resolve the scale height of debris disks at wavelengths large enough for the dust grain dynamics to be gravitationally dominant. As an interferometer, The spatial resolution is set by the longest distance between pairs of antennae, leading to a higher resolution than achievable than with past instruments. Coupled with the high

sensitivity of the ALMA antennae, the interferometer provides us with the best opportunity to resolve the vertical scale height of debris disks. We discuss our ALMA observations of the debris disk around AU Microscopii, a nearby system, in the final section of this chapter. Next, we outline the reference model used as a common reference to describe the dynamics of debris disk systems.

### 1.3 Physics of the Collisional Cascade

The canonical theoretical framework for understanding dust production in debris disks is that of the collisional cascade (Dohnanyi 1969). In this model, planetesimals within the disk are gravitationally induced into collisions, grinding each other down and generating dust at progressively smaller sizes. This eventually causes the smallest grains to become the most numerous within the disk, even as the majority of dust mass remains locked up within the largest planetesimals (Wyatt 2008; Hughes et al. 2018). The dust produced via collisions eventually becomes sufficiently small to reach the “blowout size” at which the forces of pressure from stellar radiation, winds, and/or possibly Poynting-Robertson drag overcome the strength of gravity due to the parent star (Strubbe & Chiang 2006). These forces work together to efficiently remove these smaller grains from the system, indicating that the collisional rate of the cascade must be sufficiently high to replenish the population of small grains we observe in the disk. While there is a possibility that the dust mass or flux of a debris disk is stochastic, the high incidence of bright disks that we observe suggests that the small grains remain over a sufficiently long time. The reference model for the collisional cascade follows Dohnanyi (1969), who finds that for the steady state solution to the cascade, the

differential distribution of dust grain sizes follows a power law,

$$\frac{dN}{da} \propto a^{-q} \quad (1.1)$$

where  $a$  is the size of the grain,  $N$  is the number of grains which occupy a particular size bin, and  $q \approx 3.5$ . This solution assumes that the collisional velocities and tensile strengths of bodies participating in the cascade are independent of their size. More recent numerical and analytical studies relax these restrictions, including both material and dynamical physics that more realistically match the nature of the system (Pan & Sari 2005; Gáspár et al. 2012; Pan & Schlichting 2012).

A complete theoretical treatment of the collisional cascade relies on a second parameter,  $p$ , which characterizes how the velocity dispersion  $v$  within a debris disk depends on the dust grain size,

$$v(a) \propto a^{-p} \quad (1.2)$$

As shown in Figure 1.4, the parameters  $p$  and  $q$  are together capable of differentiating between the mechanics of collisions in the cascade within the context of various dynamical regimes, as demonstrated by Pan & Schlichting (2012). Specifically, the parameter  $q$  distinguishes between collisions in the “strength” regime (upper half of Figure 1.4), in which bodies that undergo collisions are broken apart, and those within the “gravity” regime (lower left of Figure 1.4), where gravitational forces dominate the collisional mechanics of dust in the disk. Because  $q$  parametrizes the slope of the dust grain size distribution, a high value of  $q$  implies a distribution that heavily favors smaller dust grains, implying that

collisions within the cascade are destructive enough to break apart bodies. In this regime, the internal strength of bodies in the system dictates the nature of the system over that of gravity. Conversely, a lower value of  $q$  suggests a dust grain size profile that is less preferentially weighted towards smaller grains, leading to a distribution of dust grain sizes that is close to uniform. In this regime, collisional velocities between bodies is more erosive, leading to dust grain production that generates grains more similar in size. It is important to note that, while dynamics within the gravity regime require a velocity dispersion that is more uniform across dust grain sizes, collisions described by the strength regime can occur for a range of velocities, and are influenced by the total amount of small grains relative to larger grains in the system.

Since the vertical scale height directly encodes the velocity dispersion out of the midplane, we can derive a result for  $p$  by directly measuring the scale height of the disk. Deriving a value of  $q$  relies on successfully resolving the spectral index that characterizes the disk emission as a function of dust grain size. We discuss these parameters in more detail in Chapters 3 and 4. In Chapter 3, we describe the relationships that allow us to calculate values for  $q$  and  $p$  from our observations, while in Chapter 5,

## 1.4 AU Microscopii

AU Microscopii (AU Mic) is a low-mass, MIVe-type star (Torres et al. 2006) that harbors one of the brightest and closest known edge-on debris disks (Plavchan et al. 2009). First successfully resolved in scattered light by Kalas et al. (2004) following the detection of submillimeter emission (Liu et al. (2004), Figure 1.5), the disk lies a distance of  $9.91 \pm 0.11$  pc (van Leeuwen 2007), with an inclination of approximately  $90^\circ$  (Krist et al. 2005) and a flux density of  $7.1 \pm 0.2$  mJy at

1.3 mm (MacGregor et al. 2013). AU Mic therefore represents one of the optimal targets for observation at (sub)millimeter wavelengths, with an ideal inclination for probing the vertical structure of the disk. Characterizing the vertical structure is made easier by the highly symmetric nature of the AU Mic disk, whereas the most comparable target, a debris disk in  $\beta$  Pictoris, features millimeter structure that is relatively complex (Dent et al. 2014). The vertical structure itself reveals information about the dynamics of the collisional cascade. Based on the work of Pan & Schlichting (2012) it is possible to connect a measurement of the scale height to the velocity dispersion in the disk, and thereby the total mass of the largest bodies dynamically stirring the disk. Resolving the scale height at two widely separated frequencies allows for the measurement of the frequency dependence of the disk height above the midplane, which is sensitive to the internal strengths of bodies involved in the collisional cascade. This would help to distinguish between grain velocities in the disk that are destructive and those which are erosive. Finally, measuring the disk flux at the two frequencies itself helps to constrain the distribution of grain sizes in the disk.

Here we present new 0.3'' observations of the AU Mic debris disk, conducted at 450  $\mu\text{m}$  using the Atacama Large Millimeter/Submillimeter Array (ALMA). These observations complement earlier 1.4 mm observations at the same spatial resolution (Daley et al., in prep.). The 1.4 mm observations improve upon previous observations by MacGregor et al. (2013) by a factor of  $\sim 2$  in resolution, while the 450  $\mu\text{m}$  data presented here are the first observations of the disk at this wavelength. Both observations trace grains large enough to be dominated by gravitational interactions, where the effects of stellar radiation pressure are negligible (Th  bault 2009). Using these two observations, we are able to resolve the vertical structure of the AU Mic debris disk at both wavelengths for the first time (Daley et al.

in prep). From these two measurements, we are able to place constraints on the distribution of dust grain sizes in the disk, along with the internal strengths of bodies in the collisional cascade, for the first time outside of the solar system. In Chapter 2 we describe the data reduction and post-processing, and present the observations. In Chapter 3 we describe a parametric disk modeling approach to resolving the scale height at  $450\ \mu\text{m}$ , and present the results along with the resolved millimeter spectral index from the two observations. In Chapter 4 we compare our results to previous work on AU Mic, and discuss the constraints our results place on the dynamics of the collisional cascade. Chapter 5 summarizes our results and the implications for the physics of debris disk systems.

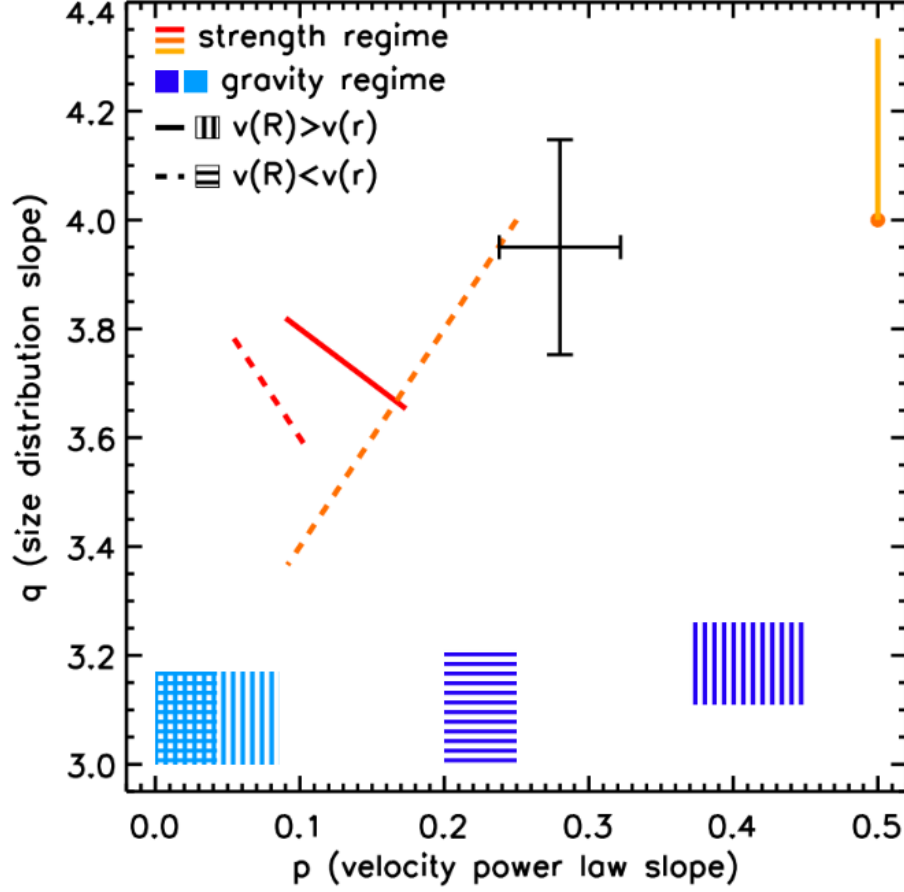


Figure 1.4: Relationship of the parameters  $p$  and  $q$  to the collisional dynamics of a debris disk, based on the work of Pan & Schlichting (2012) and created by Margaret Pan for the initial observing proposal that led to this work. Dust mass measurements from Liu (2004) and Nilsson et al. (2010). Red, yellow, and orange lines indicate the best estimates for  $p$  and  $q$  corresponding to dynamics dominated by the internal strength of bodies in the cascade, while blue regions indicate estimates in which gravitational forces dictate the nature of the collisions. Dark colors (red and dark blue) indicate catastrophic collisions, while lighter colors (orange, light blue) correspond to collisions between bodies of similar size. The yellow line implies collisions between small bodies. Error bars are prior theoretical estimates on ALMA uncertainties based on the anticipated quality of our observational data. Vertical lines in the gravity regime indicate a velocity evolution dominated by dynamical stirring from the largest bodies in the cascade, while horizontal lines indicate gravity regimes in which the velocity evolution of the system is dominated by collisional damping.



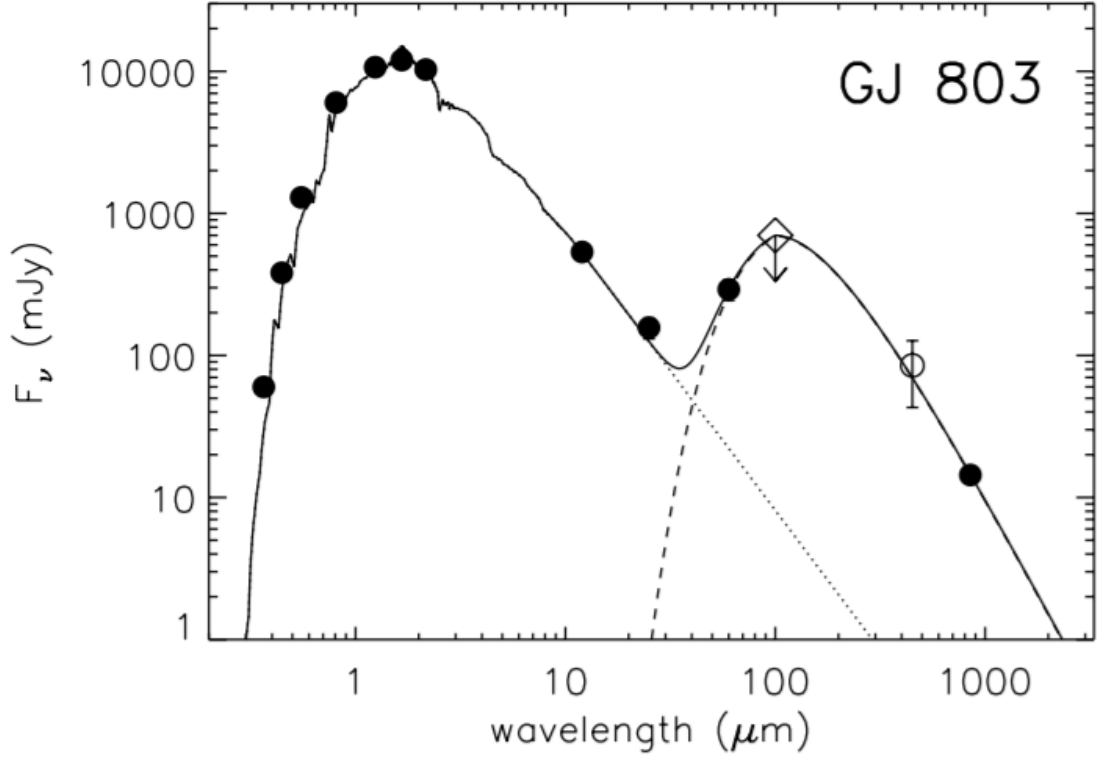


Figure 1.5: Spectra of AU Mic (GJ 803) as presented in Liu et al. (2004). The possible 450  $\mu\text{m}$  and definitive 850  $\mu\text{m}$  measurements were obtained using the SCUBA bolometer array at the James Clerk Maxwell Telescope. Filled circles indicate detections, while the open diamond is a non-detection. The open circle at 450  $\mu\text{m}$  is a non-conclusive detection. Optical data ( $\lambda \leq 8 \mu\text{m}$ ) is from SIMBAD/the *Hipparcos* catalog, while the remaining IR data is from the two-micron all sky survey. The fitted curve assumes a model in which emission from the star and IR excess are best described by a linear combination of blackbody functions.

# Chapter 2

## Observations

AU Mic was observed at  $450\ \mu\text{m}$  using the ALMA interferometer in the Atacama Desert in Chile ( $23.0234^\circ$  S by  $67.7538^\circ$  W, elevation: 5078.7 m above sea level). These data complement earlier observations of AU Mic conducted at 1.4 mm and sampled at the same spatial frequencies to enable direct comparison of the disk at the two wavelengths (Daley et al. in prep.). The observations were conducted over three separate nights on April 22, 23, and 26, 2017, separated into five scheduling blocks of between 75-100 minute intervals. The observations were conducted using the main ALMA array of 12-meter antennae, along with the band 9 receivers. Each of the observation blocks included the use of four tunable spectral windows centered at frequencies of 676.0, 678.0, 680.0, and 682.0 GHz, with a bandwidth of 2 GHz and effective channel width of  $7.01\ \text{km s}^{-1}$ , across a total of 128 channels per window. The longest baseline of the observations ( $D = 455\ \text{m}$ ) traces an angular scale of  $\sim 0.2''$  for a spatial resolution of approximately 2 au. Table 2.1 shows a summary of the observational parameters for each scheduling block.

Table 2.1: Observational Parameters for each of the five scheduling blocks composing the dataset.

Observation Block:	1	2	3	4	5
Date	04/22/2017	04/23/2017	04/23/2017	04/26/2017	04/26/2017
Antennae	45	45	45	45	45
Baseline [m]	12-455	12-455	12-455	12-455	12-455
On-Source Time [min.]	100	90	90	94	75
Flux Calibrator	J1924-2914	J1924-2914	J1733-1304	J1924-2914	J1924-2914
Gain Calibrator	J1957-3845	J1957-3845	J1957-3845	J1957-3845	J1957-3845
Bandpass Calibrator	J1924-2914	J1924-2914	J2232-1143	J1924-2914	J2232-1143
Beam Size ["]	$0.326 \times 0.244$	$0.326 \times 0.244$	$0.326 \times 0.244$	$0.326 \times 0.244$	$0.326 \times 0.244$
Beam P.A. [deg.]	87.95	87.95	87.95	87.95	87.95
Peak Flux [mJy/beam]	1.43	1.52	1.38	1.48	1.39
RMS Noise [mJy/beam]	0.20	0.26	0.24	0.23	0.23

The observations were conducted in a 3-point mosaic with 0.5-Primary Beam spacing along the position angle of the disk major axis, as measured by MacGregor et al. (2013). The raw data was processed by ALMA staff using the standard NRAO reduction and calibration pipeline implemented in the Common Astronomy Software Applications (CASA) software package (McMullin et al. 2007). We further calibrated the visibility weights using the variance around each baseline following Flaherty et al. (2017), and averaged the data in both time and bandwidth. Excessive averaging times have the potential to allow the source position to move in the interferometer reference frame by more than the synthesized beamwidth due to the changing orientation of the interferometer over the course of the observation. This causes the synthesized beam to become artificially broadened in the tangential direction, a phenomenon known as time-smearing. Similarly, bandwidth-smearing can stretch the synthesized beamwidth in the radial direction, and occurs when convolving the beam over an average channel width that is too large (Bridle & Schwab 1999). To avoid time-smearing of the synthesized

beam, we choose a time interval  $\Delta t$  such that

$$\Delta t \ll \frac{\theta_s P}{2\pi} \approx \frac{\theta_s}{\Delta\theta} \times 1.37 \times 10^4 \text{ s} \quad (2.1)$$

where  $\theta_s$  is the width of the synthesized beam,  $P$  is the rotational period of the Earth, and  $\Delta\theta$  is the largest angular resolution of the data (7.73 arcsec for  $D_{\text{min}} = 12$  m). To avoid bandwidth-smearing, a sufficient average bandwidth  $\Delta\nu$  is given by

$$\Delta\nu \ll \frac{\nu \theta_s}{\Delta\theta} \quad (2.2)$$

For a central frequency  $\nu = 667$  GHz, we were able to average all 128 channels down into a single channel without bandwidth-smearing. For time averaging, we chose a bin size of 30 seconds. We post-processed the calibrated and averaged data using both the CASA and Multichannel Image Reconstruction, Image Analysis and Display (MIRIAD) packages (McMullin et al. 2007; Sault et al. 1995).

A separate, spatially unresolved source of excess emission was found within the combined mosaic image region. Due to recent work constraining the number of expected faint background sources in a given ALMA field of view, we assume the unresolved source flux is due to a background galaxy (Hatsukade et al. 2013; Carniani et al. 2015). The total flux density of the source was determined to be approximately 1.146 mJy at ICRS coordinates  $\alpha=20^{\text{h}}45^{\text{m}}10^{\text{s}}$ ,  $\delta=-31^{\circ}20'34''$ , found by fitting a Gaussian in the image domain using the `gaussfit` function within the CASA `imview` task. The position results from this fit are included in Table 2.2. We then created a model image including only a point source with the corresponding flux density and positional offset from the image center. This

model image was subtracted from the visibilities using the MIRIAD task `uvmodel` with `options=subtract`. Upon imaging the residuals, no statistically significant flux was detected at the position of the point source, indicating that the point source model successfully subtracted the flux.

Table 2.2: Position of the background source, obtained by fitting a Gaussian to the source at each observation block in the image domain.

Observation Block	RA	RA Offset ["]	DEC	DEC Offset ["]
1	20:45:10.282	$4.676 \pm 0.057$	-31:20:33.504	$-0.049 \pm 0.041$
2	20:45:10.282	$4.673 \pm 0.069$	-31:20:33.530	$-0.074 \pm 0.053$
3	20:45:10.289	$4.757 \pm 0.043$	-31:20:33.475	$-0.019 \pm 0.035$
4	20:45:10.282	$4.671 \pm 0.043$	-31:20:33.501	$-0.041 \pm 0.032$
5	20:45:10.288	$4.748 \pm 0.042$	-31:20:33.751	$-0.291 \pm 0.036$

Each of the 5 observation blocks was centered at the expected position of the central star, and corrected for a proper motion of  $\mu[\alpha] = 2796.96 \text{ mas yr}^{-1}$ ,  $\mu[\delta] = -360.61 \text{ mas yr}^{-1}$  (van Leeuwen 2007). As AU Mic is a low-mass, M-type star, there is a high probability of a flaring event during the observations. Consequently, we checked the dataset for stellar flaring by fitting a Gaussian to the central peak in the image domain using `gaussfit` at each observation block to ensure that there was no statistically significant change in peak flux from block to block. We further examined the change in peak flux from the central source at the beginning and end of each block, looking for significant short-term variability throughout the individual observations. The results of this investigation are presented in Table 2.3, while a plot showing the flux difference across each of the observations is shown in Figure 2.1. Throughout the course of the observation, the central source flux varied from a minimum of  $0.96 \pm 0.30 \text{ mJy}$  in block 1 to a maximum of  $2.98 \pm 0.40 \text{ mJy}$  in block 3, and that the difference in flux values does not deviate by more than 3-sigma from the mean at any time during the observation. The

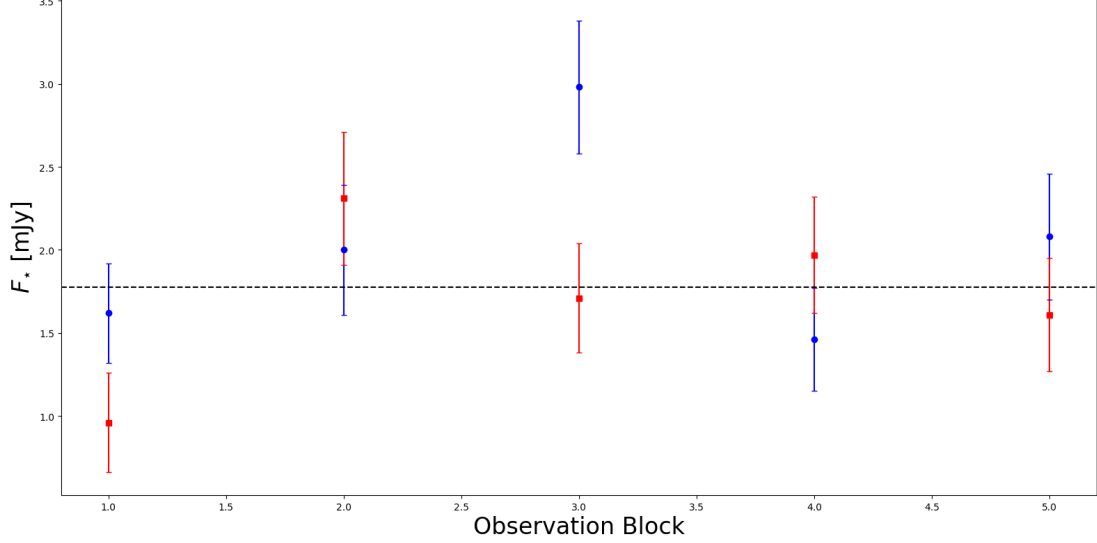


Figure 2.1: The flux from the central source for each observation block. The dashed black line shows the weighted mean flux over the course of the observations. Blue circles indicate the source flux at the start of each observation, while red squares indicate the central source flux at the end of the observation

central source flux was thus considered to be constant for the purposes of data reduction and analysis. A weighted image constructed from the final visibilities used for analysis is shown in Figure 2.2.

Table 2.3: Results from fitting a point source model to the central source in AU Mic. Peak flux values are the mean flux averaged over the first and second half of each observation block, respectively.

Block	RA	Offset	DEC	Offset	$F_p$ (Start) [mJy]	$F_p$ (End) [mJy]
1	20:45:09.918	$0.006 \pm 0.085$	-31:20:33.403	$0.052 \pm 0.066$	$1.62 \pm 0.30$	$0.96 \pm 0.30$
2	20:45:09.920	$0.041 \pm 0.055$	-31:20:33.429	$0.027 \pm 0.066$	$2.00 \pm 0.39$	$2.31 \pm 0.40$
3	20:45:09.921	$0.051 \pm 0.049$	-31:20:33.398	$0.058 \pm 0.042$	$2.98 \pm 0.40$	$1.71 \pm 0.33$
4	20:45:09.919	$0.018 \pm 0.077$	-31:20:33.435	$0.025 \pm 0.062$	$1.46 \pm 0.31$	$1.97 \pm 0.35$
5	20:45:10.224	$0.079 \pm 0.079$	-31:20:33.516	$-0.056 \pm 0.062$	$2.08 \pm 0.38$	$1.61 \pm 0.34$

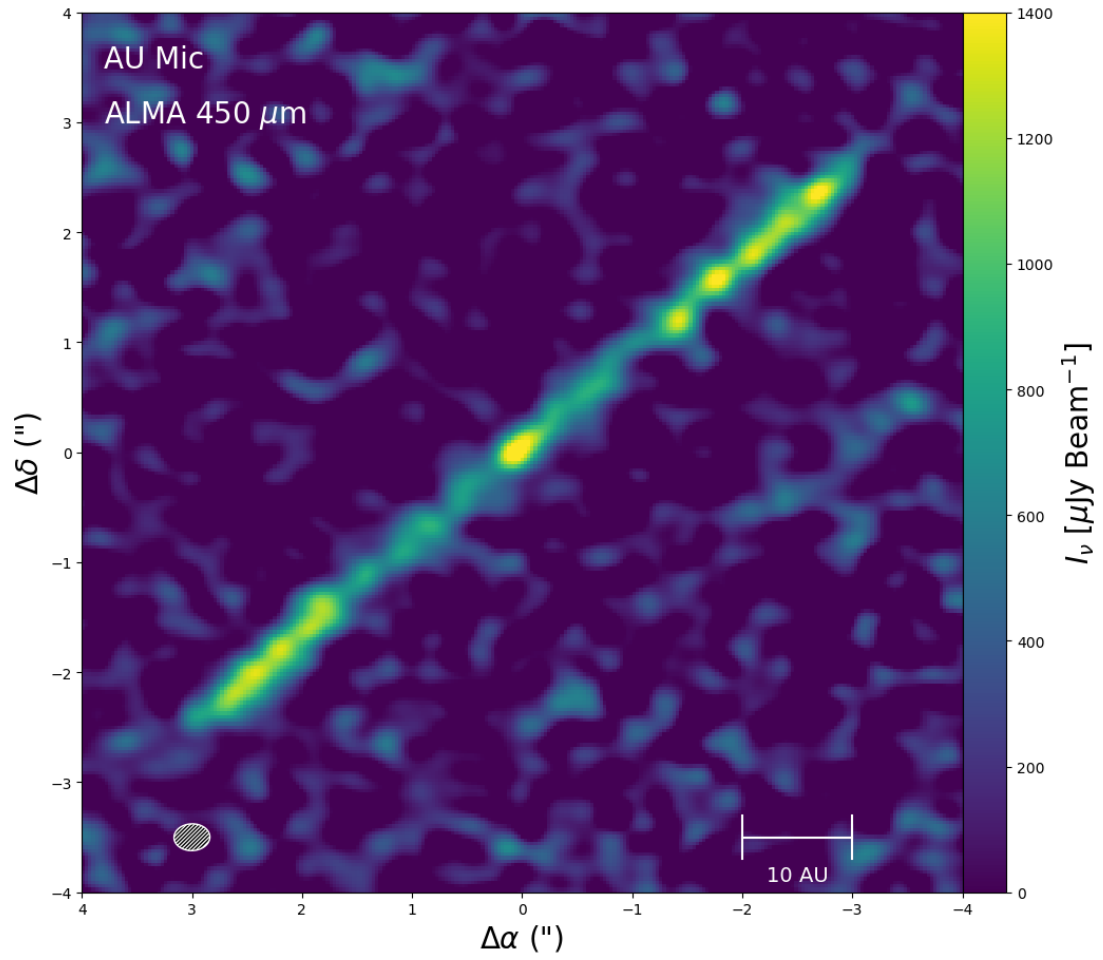


Figure 2.2: The final data image of AU Mic, observed at 450  $\mu\text{m}$  and cleaned using natural weighting, which weighs each visibility included in the dataset by its measurement uncertainty.

# Chapter 3

## Analysis

In order to characterize the features of the debris disk around AU Mic, we generated a series of parametric best fit models using the two-dimensional radiative transfer code, `DiskModel` (Flaherty et al. 2015). The software is based on the work of Rosenfeld et al. (2013), and was originally created to model gas-rich protoplanetary disks, with an underlying temperature structure following Dartois et al. (2003). Given a dust temperature and radial surface density profile, the code solves for the vertical density profile under the assumption of hydrostatic equilibrium, then generates synthetic line-of-sight observations via ray tracing, which can then be converted into model visibilities for direct comparison with the ALMA data. As the code was initially developed to generate synthetic images of the gas in protoplanetary disks under the assumption of local thermodynamic equilibrium, we adapted the code to better model tenuous, gas-poor debris disks such as AU Mic. The motivation behind this adaptation is two-fold: First, the gaseous nature of protoplanetary disks causes them to be optically thick to visible light, causing surface heating that leads to sharp radial and vertical temperature gradients that are dependent on the amount of disk flaring. Second, the gas-to-



dust ratio of protoplanetary disks is  $\sim 100 : 1$  by mass, resulting in a density structure determined by hydrostatic equilibrium (Armitage 2011). Debris disks by contrast are optically thin across the electromagnetic spectrum, yielding a dust temperature that is assumed to be dependent solely upon its distance to the central star (Wyatt 2008). Additionally, the dust mass of debris disks are comparable to or, more commonly, greater than the mass of gas, implying that the density distribution of debris disks are set by dynamics separate from hydrostatic equilibrium. We describe our parametric model for the AU Mic disk in the following section, outlining the method in which the temperature and density distributions of dust in the disk are handled.

### 3.1 Modeling the Debris Disk Around AU Mic

To determine the dust temperature distribution, we consider a dust grain of radius  $a$  within a debris disk, positioned a distance  $d$  from its parent star. The stellar flux incident on the grain is the product of its cross-sectional area and the well-known inverse-square law,

$$\phi_{\text{inc}} = \frac{L_{\star}}{4\pi d^2} \pi a^2 \quad (3.1)$$

where  $L_{\star}$  is the bolometric luminosity of the parent star. The thermal radiation emitted by the heated grain is given by the Stefan-Boltzmann law

$$\phi_{\text{out}} = 4\pi a^2 \sigma T_{\text{D}}^4 \quad (3.2)$$

where  $\sigma_{\text{SB}}$  is the Stefan-Boltzmann constant and  $T_{\text{D}}$  is the temperature of the dust. We assume that dust grains in the disk are in radiative equilibrium and feature a low surface albedo  $A \ll 1$ , such that  $\phi_{\text{inc}} = \phi_{\text{out}}$ . Setting Equations (3.1) and

(3.2) equal to one another, the dust grain temperature is given by

$$T_D = \left[ \frac{L_\star}{16\pi\sigma_{\text{SB}}d^2} \right]^{1/4} \quad (3.3)$$

By Equation (3.3), we see that the dust temperature distribution of a debris disk is independent of the size of dust grains, assuming that the grains thermally re-radiate as blackbodies. We further assume that the vertical profile of the disk is isothermal. To determine the dust density profile of the disk, we begin by normalizing the total disk mass,  $M$ , such that

$$M = \int_{r_{in}}^{r_{out}} 2\pi r \Sigma(r) dr \quad (3.4)$$

where  $\Sigma(r)$  is the surface density of the disk as a function of radius. We assume a power-law surface density structure given by

$$\Sigma_D(r) = \begin{cases} \Sigma_c r^p & \text{where } r_{in} \leq r \leq r_{out} \\ 0 & \text{otherwise} \end{cases} \quad (3.5)$$

where  $r_{in}$  and  $r_{out}$  are the disk inner and outer radius, and where  $\Sigma_c$  normalizes the dust surface density for the given disk mass. Evaluating Equation (3.4) and solving for  $\Sigma_c$ , we have that

$$\begin{aligned} M &= \int_{r_{in}}^{r_{out}} 2\pi r \Sigma(r) dr = 2\pi \Sigma_c \int_{r_{in}}^{r_{out}} r (r^p) dr \\ M &= \frac{2\pi \Sigma_c}{(p+2)} \left[ r_{out}^{(p+2)} - r_{in}^{(p+2)} \right] \\ \Sigma_c &= \frac{M (p+2)}{2\pi \left[ r_{out}^{(p+2)} - r_{in}^{(p+2)} \right]} \end{aligned} \quad (3.6)$$

The dust volume density as a function of  $r$  and height above the midplane  $z$  is given by

$$\rho_D(r, z) = \rho_D(r) \exp \left[ -\frac{z}{H(r)} \right]^2 \quad (3.7)$$

where the radial component is related to the dust surface density and scale height of the disk,  $H(r)$ , by

$$\rho_D(r) = \frac{\Sigma(r)}{\sqrt{\pi}H(r)} \quad (3.8)$$

This assumes that the vertical dust density profile of the disk is best described by a Gaussian with a standard deviation equal to  $H(r)$  at radius  $r$ , and featuring azimuthal symmetry. As for the scale height, we assume that  $H(r)$  is linear in the radial direction and scales by an aspect ratio  $h$ , such that  $h = H(r)/r$ , a common assumption in modeling debris disk structure. Figure 3.1 shows the modeled vertical dust density profile for scale heights at various radii and aspect ratio  $h = 0.032$ .

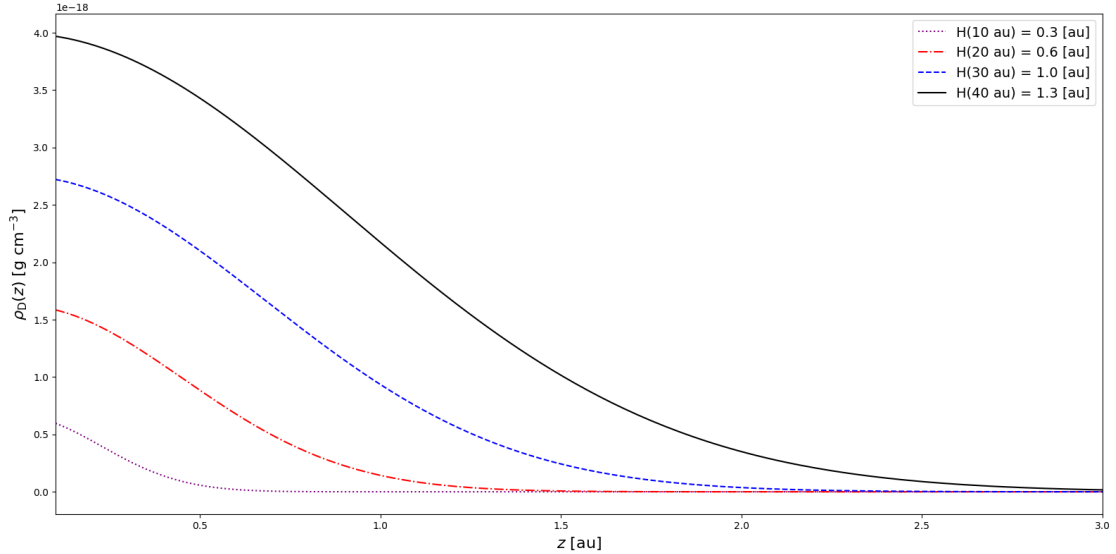


Figure 3.1: Vertical dust density distribution  $\rho_D(z)$  of a model debris disk with aspect ratio  $h = 0.032$  at a radius of 10, 20, 30, and 40 au.

Aside from the dust temperature and density profile of the disk model, we

adopt a bolometric luminosity of  $L_\star = 0.09L_\odot$  for AU Mic (Plavchan et al. 2009), and a distance to the system of  $9.91 \pm 0.10$  pc (van Leeuwen 2007). Since the central source flux returned by CASA did not vary to a significant degree, we adopt a single free parameter for the stellar flux,  $F_\star$ , in the model. We likewise leave the disk inclination ( $i$ ) and position angle (PA) with respect to the line-of-sight as free parameters in the model. The final disk model comprises 8 total free parameters, including the total mass of the disk ( $\log M$ ), sampled logarithmically to account for the sensitivity of our data to the dust mass, the inner and outer radius of the disk, ( $r_{in}$  and  $r_{out}$ , respectively), the aspect ratio corresponding to the scale height of the disk ( $h$ ), the surface brightness power law index ( $p$ ), and the median 450- $\mu\text{m}$  flux from the central star ( $F_\star$ ). We set the spatial resolution of the line-of-sight projected images produced by the model to be approximately 10% of the resolution sampled by the longest baselines in the dataset, resulting in images at 3 au per pixel. The images are then converted into model visibilities and sampled at the same spatial frequencies as the ALMA data using the MIRIAD task `uvmodel`.

Previous studies have demonstrated a degeneracy between disk radial and vertical structure, and inclination to the line of sight (Graham et al. 2007; Donaldson et al. 2013; Milli et al. 2014). For example, a debris disk that appears to have a large, “puffed-up” vertical structure may be due to a large scale height and an inclination close to  $i = 90^\circ$ , but may also be due to an inclination angle that is further from edge-on, with a scale height that is smaller (see figure 3.2). We therefore employ the use of a Markov Chain Monte Carlo (MCMC) algorithm to fully characterize these degeneracies, allowing the derivation of uncertainty on the disk scale height that accounts for the uncertainties in radial and vertical structure.

Generally, MCMC algorithms work by sampling the parameter space via ran-

dom walk such that the density of samples in a region is proportional to the probability density of the region. The sampling therefore becomes representative of the local probability density function (PDF) as the algorithm converges (Hastings 1970; Mackay 2003). This characterization of the local PDF identifies likely values for parameters via maximal probability regions in the distribution, and quantifies the uncertainties in the best fit parameters via the spread of the distribution. Lastly, parameters that are degenerate can be identified by correlated regions in their respective PDFs.

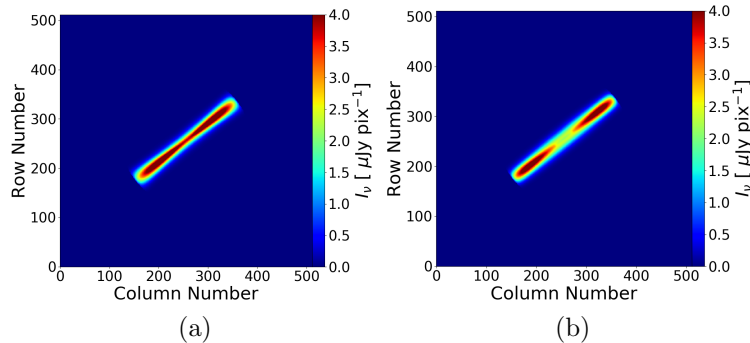


Figure 3.2: Disk models illustrating the degeneracy between inclination angle and scale height. Figure (a) shows a debris disk with  $i = 89^\circ$  and a scale height aspect ratio  $h = 0.12$ . Figure (b) shows a disk with  $i = 85^\circ$  and  $h = 0.10$ . Point source emission from a central star has not been included. While the large-scale physical structure may be hard to differentiate between the two disks, changes in the flux distribution can potentially be characterized in the course of an MCMC run, helping to successfully measure the two coupled parameters.

We determine the model parameters that best describe the debris disk around AU Mic by combining the updated modeling capabilities of `DiskModel` with the MCMC routine implemented by Foreman-Mackey et al. (2013) as the `emcee` package. The algorithm followed by `emcee` is described by Goodman & Weare (2010) and features an ensemble of MCMC samplers that are invariant under affine space translations. The performance of `emcee` is therefore independent of

the aspect ratio in probability density distributions that are highly anisotropic. We assume uniform priors for each of the 8 free parameters in our model, with a Log-uniform prior assumption to account for the logarithmic sampling of the total disk mass. Our best fit procedure employs 30 walkers over a total of 3,000 steps, drawing a total number of random samples of order  $\sim 10^5$  from the distribution. The characteristic number of steps required to allow for burn-in of the walkers in running the model ranges from approximately 200-400 steps. The final posterior distributions for each of the 8 parameters are provided in Figure 3.3. From the sharp distribution of samples for  $\log M$ ,  $p$ ,  $h$  and  $r_{\text{out}}$ , we see that the best fit values for these parameters are determined to a high degree of certainty. Conversely, the large spread of values in the PDF of  $r_{\text{in}}$  indicates that the data do not resolve the inner radius of the disk. A table of the best fit parameters in the model is provided in Table 3.1, while a plot of the imaged data, best fit convolved model, and residuals are presented in Figure 3.4.

Table 3.1: Results of the MCMC routine for each free parameter. The median values and associated uncertainties are shown, along with the best fit result for each parameter.

Parameter	Median	Best Fit
Disk Mass [ $\log M_{\odot}$ ]	$-7.64^{+0.02}_{-0.02}$	-7.65
$p$	$2.5^{+0.4}_{-0.5}$	2.4
$h$	$0.032^{+0.007}_{-0.006}$	0.030
$r_{\text{in}}$ [au]	$7^{+10}_{-5}$	4
$r_{\text{out}}$ [au]	$38.9^{+0.7}_{-0.6}$	39.1
$i$ [deg]	$88.3^{+0.5}_{-0.3}$	88.1
PA [deg]	$128.5^{+0.1}_{-0.1}$	128.5
$F_{\star}$ [ $\mu\text{Jy}$ ]	$700^{+100}_{-100}$	600
Ln Likelihood	$-2895813^{+1}_{-3}$	-2895813

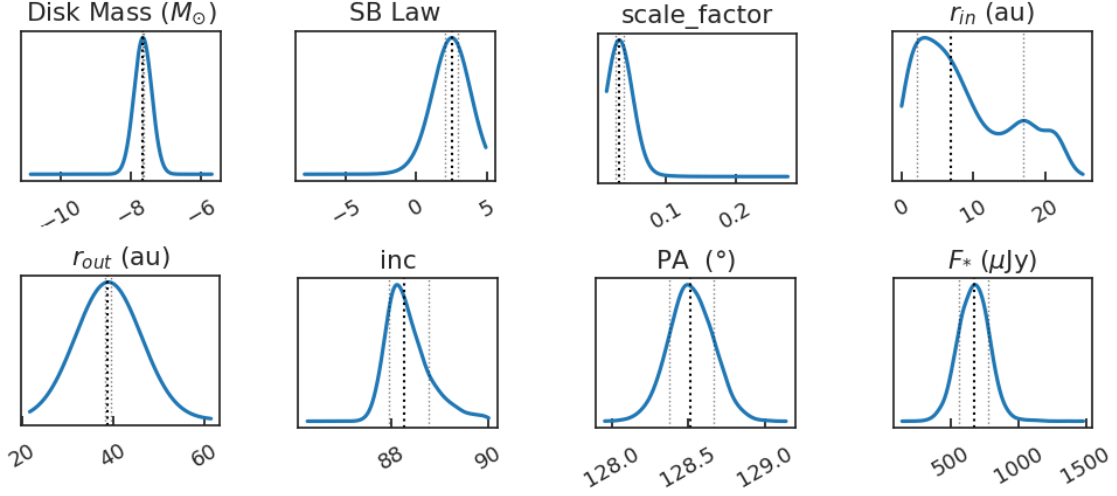


Figure 3.3: Posterior distribution functions for each of the 8 free parameters incorporated in the disk model. From left to right, each of the vertical lines intersecting the PDFs show the 16<sup>th</sup>, 50<sup>th</sup> (median), and 84<sup>th</sup> percentile values.  $p$  is represented by the PDF labeled “Surface Brightness (SB) Law,” while  $h$  is represented by the PDF labeled “scale factor.”

### 3.2 Results: Resolved Scale Height

The posterior distribution function of the aspect ratio shown in Figure 3.3 yields a value of  $h = 0.032 \pm 0.007$ , corresponding to a measured scale height of  $H = 1.2 \pm 0.3$  au at an outer disk radius of  $\sim 40$  au. The narrow width of the PDF implies that the observations are capable of resolving the scale height of AU Mic at a 4.6-sigma level of significance, even when accounting for the known degeneracy with inclination. While initially it may seem impossible to measure such a small scale height given the 2 au spatial scale implied by the longest baselines of the observations, we can justify the validity of this result in two ways. First, since  $H$  corresponds to a vertical disk height measured from the midplane, the required spatial resolution of the data to appropriately measure the scale height is  $2H = 2.4$  au, closer to the minimum spatial scale sampled by the longest baselines in the data. Second, the scale height represents the standard

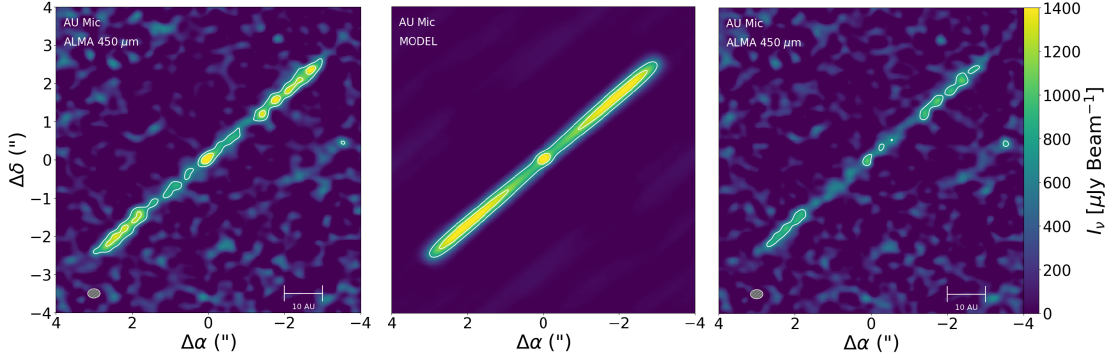


Figure 3.4: Data image, best fit convolved model image and residuals after subtraction of the model visibilities from the data. The images are sampled at the same spatial frequencies from the data, and cleaned using natural weighting. 3-sigma contours corresponding to the RMS noise of the data are overplotted for each image.

deviation of a dust distribution that is Gaussian, rather than a sharp cut-off for the vertical height of dust above the disk midplane (see Equation 3.7), allowing the full vertical structure of the disk to extend out beyond the scale height. We further verify a successful measurement of the disk scale height by fitting a disk model with a fixed aspect ratio  $h = 0.003$ , equivalent to 3% of the synthesized beam width and indicating a significantly smaller scale height by one order of magnitude. If the vertical structure of the disk is spatially unresolved, there should not be a statistically significant difference in performance between this fixed, small- $h$  model when compared against our best fit model. Figure 3.5 shows the convolved best fit model returned by the MCMC routine when holding the aspect ratio fixed at  $h = 0.003$ , and corresponding residual after subtracting the model visibilities from the data. From the residuals, it is clear that the small aspect ratio fails to completely describe the structure of the disk, particularly in the exterior ansae where the scale height is the largest. We therefore claim that the scale height is successfully resolved by the observations.



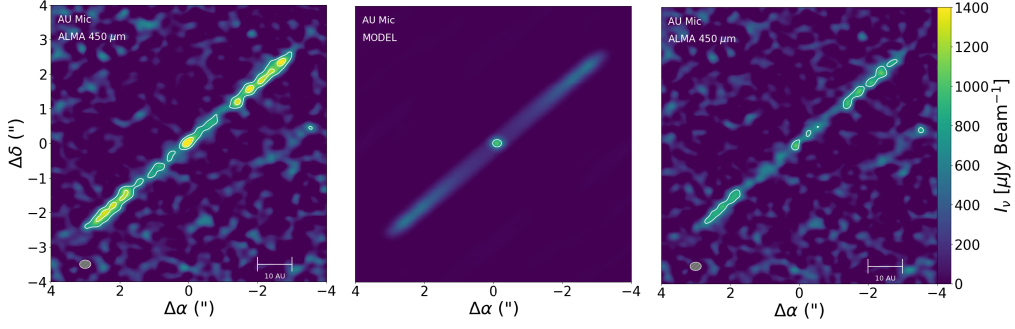


Figure 3.5: Imaged data, best fit convolved model, and residual after subtraction of the fixed aspect ratio test. 3-sigma contours are over-plotted for each image.

### 3.3 Dust Grain Size Distribution: $q$

The flux density of a debris disk at millimeter wavelengths can be described observationally by a simple power law relation,

$$F_\nu \propto \nu^{\alpha_{\text{mm}}} \quad (3.9)$$

where  $\alpha_{\text{mm}}$  is the millimeter spectral index of the disk and can be characterized by observations at two separate frequencies,

$$\alpha_{\text{mm}} = \frac{\log(F_{\nu_1}/F_{\nu_2})}{\log(\nu_1/\nu_2)} \quad (3.10)$$

With the addition of the earlier 1.4 mm observations of AU Mic conducted by Daley et al. (in prep.), we are therefore able to successfully resolve the millimeter spectral index in an attempt to look for radial variations in the grain size distribution of the debris disk. Previously, MacGregor et al. (2016) attempted to measure the integrated spectral index for AU Mic using observations with the Very Large Array telescope (VLA). Their results placed an upper limit on the AU Mic spectral index of  $< 2.46$ . Our data indicate a mean millimeter spectral index

of  $\alpha_{\text{mm}} = 0.9 \pm 0.2$ , in agreement with the upper limit set by MacGregor et al. (2016), where they were able to separate the flux from the disk and the central star (see Chapter 4). This result is lower than most of the other debris disks observed in the sample by a factor of  $\sim 2$ . Figure 3.6 shows the change in the millimeter spectral index across the spatial extent of the disk. From this plot, we see that the spectral index varies remarkably little throughout the disk, indicating that there is little to no change in the dust grain size distribution due to radial features in the disk. In the following sections, we use the results for the scale height of AU Mic, along with the resolved millimeter spectral index, to derive values for the parameters  $p$  and  $q$ .

Because the thermal emission from debris disks is in the optically thin regime, the observed flux density from a debris disk is the product of the Planck function and mass opacity (Draine 2006; Ricci et al. 2012). MacGregor et al. (2016) show that the parameter  $q$  that characterizes the slope of the dust grain size distribution may be expressed as

$$q = \frac{\alpha_{\text{mm}} - \alpha_{\text{Pl}}}{\beta_s} + 3 \quad (3.11)$$

where  $\beta_s$  is the dust opacity power-law index of dust grains smaller than the observing wavelength and determined empirically by Draine (2006) to be  $\beta_s = 1.8 \pm 0.2$ , based on modeling of astrosilicate grains.  $\alpha_{\text{Pl}}$  is the spectral index of the Planck function, and is described between two frequencies by

$$\alpha_{\text{Pl}} \approx 2 + \frac{\log \left( \frac{2k_{\text{B}}T_{\text{D}} - h\nu_1}{2k_{\text{B}}T_{\text{D}} - h\nu_2} \right)}{\log(\nu_1/\nu_2)} \quad (3.12)$$

where  $k_{\text{B}}$  is the Boltzmann constant,  $T_{\text{D}}$  is the dust temperature, and  $h$  is the Planck constant. We assume a single line-of-sight dust temperature throughout

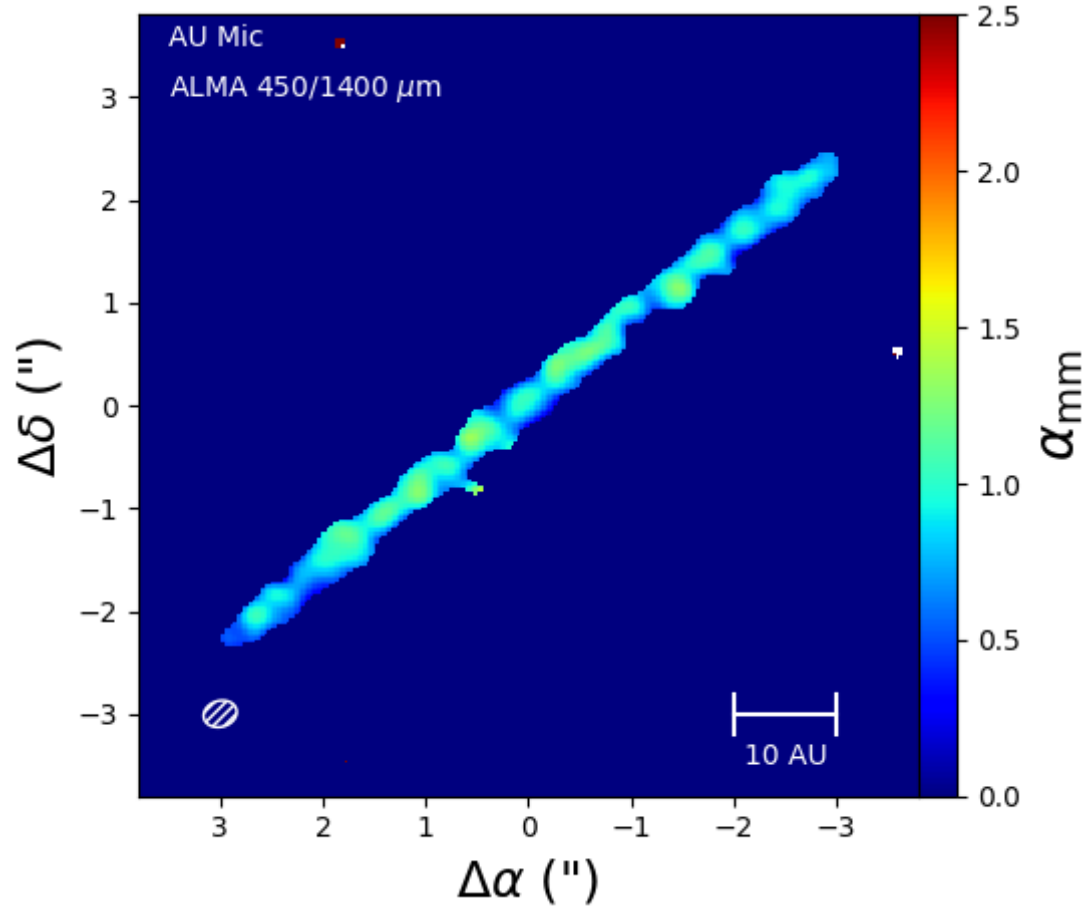


Figure 3.6: Resolved millimeter spectral index of AU Mic ( $\nu_1 = 667$  GHz /  $\nu_2 = 230$  GHz). The noisy patch in the upper left is from the unresolved background source. The data show a remarkably uniform spectral index as a function of the disk radius, and a lower average value when compared against the spectral indices of other debris disks (MacGregor et al. 2016).

the disk, and retrieve a value  $T_D \approx 23$  K from our best fit model at a radial extent of 40 au. From our measured average value of the millimeter spectral index  $\alpha_{\text{mm}} = 0.9 \pm 0.2$ , we calculate a value of  $q = 2.9 \pm 0.1$  for AU Mic. The highly uniform nature of the spectral index indicates that the dust grain size population parametrized by  $q$  remains fairly constant across all regions of the disk.

### 3.4 Velocity Dispersion in the Disk: $p$

As we discussed in Chapter 1, the vertical thickness of a debris disk directly encodes information about the dynamical properties of the disk. This is because, as small grains experience collisions from larger bodies, their orbits are more likely to become eccentric. This eccentricity,  $\langle e \rangle$  is related to an orbital inclination above the midplane of the disk,  $\langle i \rangle$ , by an equipartition such that  $\langle i \rangle \sim \langle 3 \rangle / 2$  (Th  bault 2009). Thus, a debris disk with a small aspect ratio  $h$  is likely to consist solely of small grains, while a larger aspect ratio is due to collisional excitations by some mechanism, such as a larger body (Quillen et al. 2007). For a sufficiently low orbital inclination,  $\langle i \rangle$  can be directly related to the aspect ratio as  $\langle i \rangle \sim \sqrt{2}h$ . Assuming that the velocity dispersion  $\langle \Delta v \rangle$  is to first order the escape velocity of the largest bodies in the disk (Artymowicz 1997), we can calculate the velocity dispersion using the following relation (Wetherill & Stewart 1993; Wyatt & Dent 2002):

$$\langle \Delta v \rangle \sim (\langle i^2 \rangle + 1.25 \langle e^2 \rangle)^{1/2} v_{\text{kep}}(r) \quad (3.13)$$

where  $v_{\text{kep}}(r)$  is the Keplerian velocity of the disk. The parameter  $p$  characterizes the dust grain size dependent velocity dispersion between observations at grain sizes  $a_1$  and  $a_2$ , such that

$$p = -\frac{\log(\Delta v_1 / \Delta v_2)}{\log(a_1 / a_2)} \quad (3.14)$$

---

Given our result for the aspect ratio  $h = 0.032$ , and adopting a stellar mass of  $M = 0.31 M_{\odot}$  (Plavchan et al. 2009), we calculate a velocity dispersion  $\langle \Delta v \rangle = 380 \pm 40 \text{ m s}^{-1}$  at an outer radius of 40 au. This result for the velocity dispersion corresponds to a value of  $p = 0.1 \pm 0.1$ . This measurement represents the first successful characterization of the size-dependent velocity dispersion in the disk. We discuss the implications of our results for  $p$  and  $q$  in the following chapter.

# Chapter 4

## Discussion

Results from our parametric modeling and MCMC analysis of the debris disk around AU Mic indicate that the disk holds a total dust mass of  $\sim 0.01 M_{\oplus}$ , and that the disk surface density increases following a power law relation to an outer radius that spans approximately  $\sim 40$  au. Subtraction of the best fit convolved model from the data reinforce that our model satisfactorily describes the overall structure of the disk, with no significant residuals implying the presence of additional features such as gaps or rings of dust observed at  $450 \mu\text{m}$ . Our analysis further indicates that we resolve the disk vertical structure, which corresponds to a scale height that reaches a maximum value of 1.2 au at a distance of 40 au from the disk center. In this section, we compare the results from our  $450 \mu\text{m}$  observations of AU Mic with our complementary 1.4 mm observations (Daley et al. in prep), in addition to the results of previous studies. We will further discuss the implications of our results for the parameters  $p$  and  $q$  with respect to the dynamics of the collisional cascade.

### 4.1 AU Mic Debris Disk Characteristics

Our results imply a total disk dust mass of  $(7.6 \pm 0.3) \times 10^{-3} M_{\oplus}$ , which is lower than the  $(9.6 \pm 0.1) \times 10^{-3} M_{\oplus}$  result reported by Daley et al. from the 1.4 mm ALMA observations. This could be do to the lower overall signal-to-noise ratio of the 450  $\mu\text{m}$  data compared against the 1.4 mm data ( $\text{SNR}_{\text{peak},450} = 6.04$  vs.  $\text{SNR}_{\text{peak},1.4} \sim 23$ ). These values do not take the systematic flux uncertainty of the observations into account ( $\sim 20\%$  at 450  $\mu\text{m}$ ,  $\sim 10\%$  at 1.4 mm), which could also increase the amount to which these results agree. Both of these mass values agree with previous ALMA observations at 1.4 mm by MacGregor et al. (2013), who report a dust mass of  $0.01 M_{\oplus}$ . From the first successfully resolved images of the disk in scattered light, Kalas et al. (2004) report a value of  $0.011 M_{\oplus}$  by fitting models to the AU Mic SED. Strubbe & Chiang (2006) quote a value of  $0.01 M_{\oplus}$  by first calculating a dust grain size distribution assuming a steady-state collisional cascade, and then simultaneously fitting the thermal spectrum and surface brightness profile of the AU Mic disk to *Hubble Space Telescope* (*HST*) observations carried out in the *V* and *H* bands. A contemporaneous study by Augereau & Beust (2006) initially reports a value of  $1.46 \times 10^{-4} M_{\oplus}$  by inverting the observed surface brightness profile of AU Mic. However, the authors later find a value of  $7 \times 10^{-3} M_{\oplus}$  by relaxing their constraints on the dust grain size distribution in order to better reproduce the AU Mic SED, a result that agrees well with our own. At 850  $\mu\text{m}$ , Liu et al. (2004) report a value of  $0.011 M_{\oplus}$  from an unresolved detection using the SCUBA bolometer array at JCMT. This result is confirmed by Metchev et al. (2005) by modeling *H*-band observations obtained using the adaptive optics system of the Keck telescope. Matthews et al. (2015) performed low resolution imaging of the disk at 70, 160, 250, 450, 500, and 850

$\mu\text{m}$ , resolving the disk at 70, 160, and 450  $\mu\text{m}$  and detecting thermal emission from the disk halo for the first time. The results from this study include a value of  $0.01M_{\oplus}$  with 20% uncertainty. Our results at both 450  $\mu\text{m}$  and 1.4 mm are therefore widely consistent with published values for the total disk mass.

Our 450  $\mu\text{m}$  results for the geometrical properties of the AU Mic disk agree similarly well with the results at 1.4 mm, in addition to values from the literature. We report a median PA for the disk of  $128^{\circ}.5 \pm 0.1$ , which agrees with the 1.4 mm PA of  $128^{\circ}.47 \pm 0.07$  to within the uncertainties. We find the disk to be close to edge-on, with a median inclination  $i = 88^{\circ}.3^{+0.5}_{-0.3}$ , which agrees with the 1.4 mm value of  $i = 88^{\circ}.6^{+0.4}_{-0.3}$ . Our results for the PA of AU Mic at both wavelengths are in agreement with past measurements reported by Krist et al. (2005) and MacGregor et al. (2013). However, the optical PA of  $127^{\circ}.8 \pm 0.2$  reported by Schneider et al. (2014), obtained using the Space Telescope Imaging Spectrograph (STIS) on *HST* for a disk radius between 50 and 100 au, does not agree with our result at a 3.1-sigma level of significance. Metchev et al. (2005) reports an optical PA of  $129^{\circ}.8 \pm 0.2$  for  $r < 50$  au, in disagreement with our result at a significance level of 4.6-sigma. Observations in scattered light further note an offset between the two disk midplanes, an asymmetry that we do not observe at 450  $\mu\text{m}$  (Kalas et al. 2004; Liu et al. 2004; Metchev et al. 2005). However, as scattered light observations probe sub-micron sized grains that are susceptible to radiation pressure, the mechanics that drive disk features in scattered light are separate from the gravity-dominated physics responsible for what we observe at longer wavelengths (Wyatt et al. 1999). It is therefore not unreasonable that our results for the (sub)millimeter PA of the AU Mic disk do not agree with the PA measured in the optical regime, nor is it unreasonable that the disk does not appear to feature an asymmetric midplane in our data. Our results for the



inclination angle do match previous results at optical wavelengths to within error (Krist et al. 2005; Metchev et al. 2005).

Our result for the outer radius of the disk,  $r_{\text{out}} = 39.9^{+0.7}_{-0.6}$  au, differs with the 1.4 mm value of  $42.3^{+0.4}_{-0.5}$  at a level ranging from 2.8 to 3.3-sigma. This implies that the 450  $\mu\text{m}$  distribution of dust may not extend out to the same radial extent of the 1.4 mm dust. These results both match a previously measured 1.4 mm result reported by MacGregor et al. (2013) as  $40.3 \pm 0.4$  au. However, our value for the inner radius,  $r_{\text{in}} = 7^{+10}_{-5}$ , is not well constrained, and the PDF returned by our MCMC analysis indicates that the inner radius of the data is not well sampled (see figure 3.3). We therefore do not believe we have resolved the innermost radial structure of the disk. Daley et al. report an inner radius at  $r_{\text{in}} = 23.8^{+0.6}_{-0.9}$ . While our result does not agree well with the 1.4 mm result, we note that our maximum possible inner radius of the disk approaches the 1.4 mm value due to the large uncertainty in our result. Our result agrees more closely with the value of  $8.8^{+11}_{-1.0}$  au reported by MacGregor et al. (2013), but we note that this result is similarly not well-constrained. Our analysis implies that the dust surface density of the disk increases with radius following a power law  $\Sigma \propto \Sigma_C r^p$ , with  $p = 2.5^{+0.4}_{-0.5}$ . This result agrees well with the previous value reported by MacGregor et al. (2013) of  $p = 2.32^{+0.21}_{-0.31}$ . However, the high-resolution 1.4 mm observations prefer a value of  $p = 0.9^{+0.5}_{-0.4}$ . Daley et al. (in prep.) note that the discrepancies are due to a bi-modality in the solutions of  $r_{\text{in}}$ ,  $r_{\text{out}}$ , and  $p$ . The authors suggest that these two solutions are likely attributable to symmetric emission features interior to 10 au that are detected in 1.4 mm at the 3-sigma level of significance that are not detected at the SNR of the 450  $\mu\text{m}$  observations. The authors further posit that an annulus of material could explain these features, where the resolution obtained by MacGregor et al. (2013) was not sufficient to resolve these interior features. It

is possible that we do not observe this annulus due to the increased susceptibility of  $450\ \mu\text{m}$  grains to be removed from the interior section of the disk, via accretion onto the parent star, photodissociation, or some other means.

Our analysis of the vertical profile of AU Mic indicates an aspect ratio for the disk of  $h = 0.032^{+0.007}_{-0.006}$  at a reference radius of 40 au, corresponding to a measured scale height of  $H = 1.2 \pm 0.3$  au. These results agree closely with the 1.4 mm observations, which suggest an aspect ratio and scale height of  $h = 0.031 \pm 0.005$  and  $H = 1.2 \pm 0.2$  au, respectively. As we discussed in the previous chapter, Thébault (2009) argues that the observed vertical profile of a debris disk in scattered light can vary significantly from the vertical profile at FIR and millimeter wavelengths. This is because smaller dust grains are susceptible to increased orbital eccentricities induced by stellar winds and radiation pressure at observed wavelengths  $\lambda < 50\ \mu\text{m}$ . Consequently, the aspect ratio and corresponding scale height of AU Mic are reported at a wide range of values in the literature depending on the observational methods and reference wavelength. Thébault (2009) claims a minimum aspect ratio  $h = 0.04 \pm 0.02$  at wavelengths shorter than  $50\ \mu\text{m}$ , which is within the limits of our observations despite the difference in wavelength. In scattered light, Krist et al. (2005) fits a Lorentzian vertical density distribution profile to *VBI*-band observations obtained by *HST* using the coronagraph feature of the High Resolution Camera (HRC). The authors find a FWHM disk midplane thickness between 2.5-3.5 au at a radius interior to 50 au, that increases to between 6.5-9 au at  $r \sim 75$  au. Metchev et al. (2005) estimate a FWHM of between 4-4.4 au at a radius of  $r \sim 40$  au from Keck *H*-band observations. The authors further perform parametric disk modeling to compare against *H* and *R* band observations assuming a fixed scale height  $H = 0.8$  au at  $r = 40$  au, and find that their models satisfactorily describe the observations. While MacGregor et al. (2013) do

not quote a scale height or aspect ratio due to their 1.4 mm observations being vertically unresolved, Schüppler et al. (2015) place an upper limit of 0.05 on the opening angle by measuring the vertical profile imaged from the MacGregor et al. (2013) data. The authors further estimate an opening angle of 0.03 directly from the STIS image presented in (Schneider et al. 2014). Finally, the authors examine SED modeling of the disk, and find that an opening angle of 0.05 best describes the SED of the disk, although it fails to fully reproduce the short wavelength ( $< 70 \mu\text{m}$ ) regime of the SED. The authors point out that an opening angle of 0.05 agrees with the values of 0.04-0.07 derived from IR observations (Krist et al. 2005; Metchev et al. 2005).

We therefore find that our results for the aspect ratio and scale height at  $450 \mu\text{m}$  and 1.4 mm are within the uncertainties of values previously quoted in the literature. While our measured values are generally lower than past results, we expect this to be the case based on the dynamics of larger grains, where gravitational forces dominate over the effects of stellar winds and radiation pressure (Thébault 2009).

## 4.2 Constraints on the Collisional Cascade: $q$ and $p$

From our ALMA observations obtained at  $450 \mu\text{m}$  and at 1.4 mm, we are able to resolve the millimeter spectral index that characterizes the SED between the two frequencies,  $\alpha_{\text{mm}}$ . We are further able to trace variations in  $\alpha_{\text{mm}}$  across the radius of the disk, in order to determine whether there is any radial dependence of the spectral index. We find a millimeter spectral index value  $\alpha_{\text{mm}} = 0.9 \pm 0.2$ . Wilner et al. (2012) extrapolate infer a spectral index at 350/1300  $\mu\text{m}$  to be close to 2.0 using observations with the Submillimeter Array (SMA). Matthews et al. (2015) compare the 350/1300  $\mu\text{m}$  and 450/1300  $\mu\text{m}$  flux ratios and find values for

$\alpha$  ranging from  $\sim 1.5 - 2.0$ . MacGregor et al. (2016) use Very Large Array (VLA) observations of 15 debris disks coupled with millimeter emission obtained with SMA or ALMA and arrive at an upper limit on the spectral index of AU Mic of  $\alpha_{\text{mm}} < 1.69$ , which agrees with our result. The millimeter spectral indices of the other disks in the MacGregor et al. (2016) sample largely range from  $\sim 2.5-3.0$ , with the closest resolved spectral index to our result being the HD141569 debris disk, with  $\alpha = 1.63$ . Our result for the resolved  $450/1400 \mu\text{m}$  spectral index is therefore among the lowest recorded mm spectral indices for debris disks. This raises the possibility that AU Mic may not be representative of a typical debris disk. However, AU Mic is the only M-type star included in the MacGregor et al. (2016) sample, and our result could be representative of debris disks around the lowest-mass stars.

In our analysis, we discussed how the millimeter spectral index encodes information about the distribution of dust grain sizes within a debris disk. In particular, we can determine the slope of the grain size distribution,  $q$ , from  $\alpha_{\text{mm}}$  and from the Planck spectral index,  $\alpha_{\text{Pl}}$ , which is calculated by inferring a single line-of-sight temperature of  $T_{\text{D}} = 23 \text{ K}$  at the outer disk radius. We calculate a value of  $q = 2.9 \pm 0.1$ , which agrees with the upper limit imposed by MacGregor et al. (2016) of  $q < 3.31$ . However, the authors calculate values for  $q$  by complementing their sample of 15 disks with Australia Telescope Compact Array data obtained by Ricci et al. (2012, 2015) and find ranges for  $\langle q \rangle$  between 2.84 and 3.64, with a weighted mean value  $\langle q \rangle = 3.36 \pm 0.02$ . This result agrees with the mean value reported by Ricci et al. (2015a) of  $\langle q \rangle = 3.42 \pm 0.03$  for five of the disks included in the MacGregor et al. (2016) sample. Our own lower result for  $q$  indicates a shallower size distribution of dust grains within the AU Mic debris disk than may be found within debris disks on average.

In the seminal study of the steady state collisional cascade model, Dohnanyi (1969) arrives at a value the slope of the dust grain size distribution of  $q = 3.5$  by assuming that the collisional velocities and tensile strengths of dust grains in the cascade are independent of grain size. Subsequent numerical work by Gáspár et al. (2012) and Pan & Schlichting (2012) have found a steeper slope at  $q \sim 4$  by incorporating a size-dependent velocity distribution. Conversely, Pan & Sari (2005) arrive at a value of  $q \sim 3$  by colliding Kuiper Belt analogs with a reduced tensile strength. In their model, which additionally includes a steady state size distribution, Pan & Schlichting (2012) find that a value  $3 \leq q < 3.17$  indicates that collisions in the cascade occur between bodies of similar sizes, and that the dynamics of the cascade are within the gravity-dominated regime. This suggests that the internal strength of bodies in the AU Mic cascade do not play a significant role in the dynamics of collisional cascade, compared against the influence of gravitational forces.

With the  $0.3''$  angular resolution of our data at both  $450 \mu\text{m}$  and  $1.4 \text{ mm}$ , we are able to successfully resolve the vertical scale height of the AU Mic debris disk. From the data, we measure an aspect ratio of  $h = 0.032^{+0.007}_{-0.006}$ , leading to a scale height of  $H = 1.2$  at the  $40 \text{ au}$  radial extent of the debris disk. Following the relation described by Wetherill & Stewart (1993) and Wyatt & Dent (2002), we use our measured aspect ratio to calculate the velocity dispersion of bodies in the disk which participate in the collisional cascade. We find a dispersion velocity  $\langle \Delta v \rangle = 380 \pm 40 \text{ m s}^{-1}$ , which agrees with the velocity dispersion reported by Daley et al. (in prep) of  $\langle \Delta v \rangle = 340 \pm 60 \text{ m s}^{-1}$ . As we discussed in the previous chapter, the parameter  $p$  describes how the velocity dispersion within the disk is dependent upon particle size,

$$\langle \Delta v \rangle \propto a^{-p} \quad (4.1)$$

We can therefore express the grain size-dependent velocity dispersion within the AU Mic debris disk characterized by observations at grains of size  $a_1$  and  $a_2$  by

$$p \propto -\frac{\log(\langle \Delta v_1 \rangle / \langle \Delta v_2 \rangle)}{\log(a_1/a_2)} \quad (4.2)$$

From this relation, we calculate a value  $p = 0.1 \pm 0.1$ , which indicates that the velocity dispersion within the disk features little to no dependence on dust grain size. Following the work of Pan & Schlichting (2012), we find that our result for  $p$  is below the minimum threshold for collisional velocities that are catastrophic within the gravity regime ( $0.20 < p_{\min} < 0.34$ ). This suggests that collisional velocities between bodies participating in the cascade are not destructive, but erosive, with dust grains wearing each other down rather than breaking each other apart to produce smaller grains. Our result for  $p$  reinforces the implication that the tensile strengths of bodies are low enough to be insignificant based on our result for  $q$ .

Comparison of our results of both  $p$  and  $q$  with the work of Pan & Schlichting (2012) provides a complete description of the dynamics within the AU Mic collisional cascade. We find a shallow distribution of dust grain sizes, with collisional velocities between these similar-sized bodies that are erosive and dominated by gravitational forces. This indicates that bodies within the cascade are fractal agglomerates of accreted material that are easily destroyed by collisions, rather than hard, spherical pebbles modeled by Dohnanyi (1969). We have therefore characterized the dynamics of the collisional cascade for a debris disk other than our own Kuiper belt for the first time.

# Chapter 5

## Conclusion

In this work, we have presented new 450  $\mu\text{m}$  ALMA observations of the debris disk around AU Mic. These observations are in complement to 1.4 mm observations obtained by Daley et al. (in prep) at the same spatial frequencies, and both feature an angular resolution that improves upon previous observations of the disk by a factor of  $\sim 2$ , sufficient to resolve the vertical structure of the disk for the first time. Parametric 2D modeling coupled with MCMC analysis suggests that the vertical structure of the disk is resolved, with the vertical profile of the disk best described by an aspect ratio  $h = 0.032^{+0.007}_{-0.006}$ . This corresponds to a scale height  $H = 1.2 \pm 0.3$  au at the  $\sim 40$  au radial extent of the disk with a 4.6-sigma level of confidence. This result is in strong agreement with the aspect ratio measured at 1.4 mm of  $h = 0.031 \pm 0.005$ , implying a scale height of  $H = 1.2 \pm 0.2$  au at a distance of 40 au from the center of the disk. Further analysis of this result indicates that a disk model corresponding to an unresolved scale height does not describe the data as well as a model that assumes resolved vertical structure. This implies that our reported value of the scale height is not a lower limit, but a measured result. Our data resolves the millimeter spectral index between the

450  $\mu\text{m}$  and 1.4 mm observations, where we find a mean value  $\alpha_{\text{mm}} = 0.9 \pm 0.2$ , with little to no variation throughout the radial extent of the disk. Following the work of Draine (2006) and Ricci et al. (2012), our result for the millimeter spectral index lead to a calculated value for the parameter  $q = 2.9 \pm 0.1$ . From our measured aspect ratio, we follow the method outlined by Thébault (2009) to calculate the velocity dispersion in the disk, and find that  $\langle \Delta v \rangle = 370 \pm 40 \text{ m s}^{-1}$  at 40 au. This result agrees with the result reported by Daley et al. for the 1.4 mm observations at 40 au,  $\langle \Delta v \rangle = 360 \pm 60 \text{ m s}^{-1}$ . Comparison of the results indicates that the variation in the velocity dispersion across grain sizes is best described by a power law with index  $p = 0.1 \pm 0.1$ . This represents the first measurement of the frequency-dependent velocity dispersion within the debris disk.

Following the work of Pan & Schlichting (2012), we are able to connect our results for the parameters  $p$  and  $q$  to the internal strengths of bodies in the collisional cascade, and constrain the overall population of dust grain sizes, respectively. Our result for  $p$  indicates that the collisional velocities in the disk are lower than the destructive velocities predicted by the steady state solution to the collisional cascade model (Dohnanyi 1969), and that the overall velocity dispersion exhibited by the disk remains constant across different grain size regimes. Our result for  $q$  indicates that there is a smaller number of larger grains responsible for replenishing the dust population observed in the disk via collisions. The two parameters together strongly suggest that the dynamics of the collisional cascade in AU Mic are within the gravity regime, where the strength of gravitational forces dominates the physics of collisions over the tensile strength of participant bodies. Coupled with the lower collisional velocities, our results suggest that the morphology of dust grains is not best modeled by compact spheres, as modeled by Dohnanyi (1969), but rather fractal agglomerates with a low internal strength, that fragment more



easily to produce smaller grains during collisions.

Our results show that ALMA is capable of resolving the vertical structure of nearby debris disks in order to constrain the physics of the collisional cascade for the first time outside of the Solar System. The results lead to several additional questions worth exploring in future work. Because AU Mic is a low-mass, M-type star, the dynamics of the collisional cascade in its debris disk may not be applicable to higher-mass stars. With a system age of  $\sim 20$  Myr, Au Mic harbors a younger debris disk than can be found around other stars. It is therefore possible to trace the collisional cascade dynamics across disks of various ages to see if there is an evolution in the mechanics over time. Debris disks with significantly different masses or radii could also potentially lead to different physical mechanisms, due to the overall distribution of dust and planetesimals within the disk. Each of these factors could play a role in the nature and number of planets ultimately formed in a system. By applying the methods presented in this work to observations of other debris disks, we can build a representative sample of collisional cascade parameters to answer these questions.

# Bibliography

- Armitage, P. J. 2011, *ARA&A*, 49, 195
- Artymowicz, P. 1997, *Annual Review of Earth and Planetary Sciences*, 25, 175
- Augereau, J.-C., & Beust, H. 2006, *A&A*, 455, 987
- Aumann, H. H., Gillett, F. C., Beichman, C. A., et al. 1984, *ApJL*, 278, L23
- Backman, D. E., & Paresce, F. 1993, in *Protostars and Planets III*, ed. E. H. Levy & J. I. Lunine, 1253–1304
- Beckwith, S. V. W., Sargent, A. I., Chini, R. S., & Guesten, R. 1990, *AJ*, 99, 924
- Bohlin, R. C., Savage, B. D., & Drake, J. F. 1978, *ApJ*, 224, 132
- Bonnor, W. B. 1956, *MNRAS*, 116, 351
- Bridle, A. H., & Schwab, F. R. 1999, in *Astronomical Society of the Pacific Conference Series*, Vol. 180, *Synthesis Imaging in Radio Astronomy II*, ed. G. B. Taylor, C. L. Carilli, & R. A. Perley, 371
- Carniani, S., Maiolino, R., De Zotti, G., et al. 2015, *A&A*, 584, A78
- Chambers, J. E. 2010, *Icarus*, 208, 505
- Chen, C. H., Patten, B. M., Werner, M. W., et al. 2005, *ApJ*, 634, 1372

- Clarke, C. J., Gendrin, A., & Sotomayor, M. 2001, MNRAS, 328, 485
- Dartois, E., Dutrey, A., & Guilloteau, S. 2003, A&A, 399, 773
- Dent, W. R. F., Wyatt, M. C., Roberge, A., et al. 2014, Science, 343, 1490
- Dohnanyi, J. S. 1969, JGR, 74, 2531
- Donaldson, J. K., Lebreton, J., Roberge, A., Augereau, J.-C., & Krivov, A. V. 2013, ApJ, 772, 17
- Draine, B. T. 2006, ApJ, 636, 1114
- Dullemond, C. P., Dominik, C., & Natta, A. 2001, ApJ, 560, 957
- Dullemond, C. P., & Monnier, J. D. 2010, ARA&A, 48, 205
- Durisen, R. H., Gingold, R. A., Tohline, J. E., & Boss, A. P. 1986, AApJ, 305, 281
- Dutrey, A., Guilloteau, S., & Simon, M. 1994, A&A, 286, 149
- Ebert, R. 1955, Z. Astrophys., 37, 217
- Eiroa, C., Marshall, J. P., Mora, A., et al. 2013, A&A, 555, A11
- Elmegreen, B. G. 2012, in IAU Symposium, Vol. 284, The Spectral Energy Distribution of Galaxies - SED 2011, ed. R. J. Tuffs & C. C. Popescu, 317–329
- Flaherty, K. M., Hughes, A. M., Rosenfeld, K. A., et al. 2015, ApJ, 813, 99
- Flaherty, K. M., Hughes, A. M., Rose, S. C., et al. 2017, ApJ, 843, 150
- Foreman-Mackey, D., Hogg, D. W., Lang, D., & Goodman, J. 2013, PASP, 125, 306

- Gáspár, A., Psaltis, D., Rieke, G. H., & Özel, F. 2012, *ApJ*, 754, 74
- Gillett, F. C. 1986, in *Astrophysics and Space Science Library*, Vol. 124, *Light on Dark Matter*, ed. F. P. Israel, 61–69
- Goodman, J., & Weare, J. 2010, *Communications in Applied Mathematics and Computational Science*, Vol. 5, No. 1, p. 65-80, 2010, 5, 65
- Graham, J. R., Kalas, P. G., & Matthews, B. C. 2007, *ApJ*, 654, 595
- Greene, T. P. 2001, *American Scientist*, 89, 316. <http://www.jstor.org/stable/27857500>
- Haisch, Jr., K. E., Lada, E. A., & Lada, C. J. 2001, *ApJL*, 553, L153
- Hastings, W. K. 1970, *Biometrika*, 57, 97. <http://www.jstor.org/stable/2334940>
- Hatsukade, B., Ohta, K., Seko, A., Yabe, K., & Akiyama, M. 2013, *ApJL*, 769, L27
- Hoyle, F. 1953, *ApJ*, 118, 513
- Hughes, A. M., Duchene, G., & Matthews, B. 2018, *ArXiv e-prints*, arXiv:1802.04313
- Jeans, J. 1929, *Astronomy and Cosmogony* (Cambridge University Press (2009)). <https://books.google.com/books?id=-ZqhAg5fpTYC>
- Kalas, P., Liu, M. C., & Matthews, B. C. 2004, *Science*, 303, 1990
- Kenyon, S. J., & Bromley, B. C. 2004, *AJ*, 128, 1916
- . 2006, *AJ*, 131, 1837

- Kokubo, E., Ida, S., & Makino, J. 1998, in LPI Contributions, Vol. 957, Origin of the Earth and Moon, 20
- Krist, J. E., Ardila, D. R., Golimowski, D. A., et al. 2005, *AJ*, 129, 1008
- Krumholz, M. R. 2011, in American Institute of Physics Conference Series, Vol. 1386, American Institute of Physics Conference Series, ed. E. Telles, R. Dupke, & D. Lazzaro, 9–57
- Larson, R. B. 1981, *MNRAS*, 194, 809
- . 2003, *Reports on Progress in Physics*, 66, 1651
- Liu, M. C. 2004, *Science*, 305, 1442
- Liu, M. C., Matthews, B. C., Williams, J. P., & Kalas, P. G. 2004, *apJ*, 608, 526
- Lynden-Bell, D., & Pringle, J. E. 1974, *MNRAS*, 168, 603
- MacGregor, M. A., Wilner, D. J., Rosenfeld, K. A., et al. 2013, *ApJL*, 762, L21
- MacGregor, M. A., Wilner, D. J., Chandler, C., et al. 2016, *ApJ*, 823, 79
- Mackay, D. J. C. 2003, *Information Theory, Inference and Learning Algorithms*, 640
- Mamajek, E. E. 2009, in American Institute of Physics Conference Series, Vol. 1158, American Institute of Physics Conference Series, ed. T. Usuda, M. Tamura, & M. Ishii, 3–10
- Matthews, B. C., Kennedy, G., Sibthorpe, B., et al. 2015, *ApJ*, 811, 100
- McKee, C. F., & Ostriker, E. C. 2007, *ARA&A*, 45, 565

- McMullin, J. P., Waters, B., Schiebel, D., Young, W., & Golap, K. 2007, in *Astronomical Society of the Pacific Conference Series*, Vol. 376, *Astronomical Data Analysis Software and Systems XVI*, ed. R. A. Shaw, F. Hill, & D. J. Bell, 127
- Metchev, S. A., Eisner, J. A., Hillenbrand, L. A., & Wolf, S. 2005, *ApJ*, 622, 451
- Milli, J., Lagrange, A.-M., Mawet, D., et al. 2014, *A&A*, 566, A91
- Montesinos, B., Eiroa, C., Krivov, A. V., et al. 2016, *A&A*, 593, A51
- Nilsson, R., Liseau, R., Brandeker, A., et al. 2010, *A&A*, 518, A40
- Pan, M., & Sari, R. 2005, *Icarus*, 173, 342
- Pan, M., & Schlichting, H. E. 2012, *ApJ*, 747, 113
- Perri, F., & Cameron, A. G. W. 1974, *Icarus*, 22, 416
- Plavchan, P., Werner, M. W., Chen, C. H., et al. 2009, *ApJ*, 698, 1068
- Quillen, A. C., Morbidelli, A., & Moore, A. 2007, *MNRAS*, 380, 1642
- Ricci, L., Carpenter, J. M., Fu, B., et al. 2015a, *ApJ*, 798, 124
- Ricci, L., Maddison, S. T., Wilner, D., et al. 2015b, *ApJ*, 813, 138
- Ricci, L., Testi, L., Maddison, S. T., & Wilner, D. J. 2012, *A&A*, 539, L6
- Roberge, A., & Kamp, I. 2010, *Protoplanetary and Debris Disks*, ed. S. Seager, 269–295
- Rosenfeld, K. A., Andrews, S. M., Hughes, A. M., Wilner, D. J., & Qi, C. 2013, *ApJ*, 774, 16

- Safronov, V. S., & Zvjagina, E. V. 1969, *Icarus*, 10, 109
- Sault, R. J., Teuben, P. J., & Wright, M. C. H. 1995, in *Astronomical Society of the Pacific Conference Series*, Vol. 77, *Astronomical Data Analysis Software and Systems IV*, ed. R. A. Shaw, H. E. Payne, & J. J. E. Hayes, 433
- Schneider, G., Grady, C. A., Hines, D. C., et al. 2014, *AJ*, 148, 59
- Schüppler, C., Löhne, T., Krivov, A. V., et al. 2015, *A&A*, 581, A97
- Shu, F. H., Adams, F. C., & Lizano, S. 1987, *ARA&A*, 25, 23
- Strubbe, L. E., & Chiang, E. I. 2006, *ApJ*, 648, 652
- Terebey, S., Shu, F. H., & Cassen, P. 1984a, *ApJ*, 286, 529
- . 1984b, *ApJ*, 286, 529
- Thébault, P. 2009, *A&A*, 505, 1269
- Thébault, P., & Augereau, J.-C. 2007, *A&A*, 472, 169
- Torres, C. A. O., Quast, G. R., da Silva, L., et al. 2006, *A&A*, 460, 695
- Tricco, T. S., Price, D. J., & Laibe, G. 2017, *MNRAS*, 471, L52
- van Leeuwen, F. 2007, *A&A*, 474, 653
- Wetherill, G. W., & Stewart, G. R. 1993, *Icarus*, 106, 190
- Williams, J. P., & Cieza, L. A. 2011, *ARA&A*, 49, 67
- Wilner, D. J., Andrews, S. M., MacGregor, M. A., & Hughes, A. M. 2012, *ApJL*, 749, L27

Wyatt, M. C. 2008, *ARA&A*, 46, 339

Wyatt, M. C., & Dent, W. R. F. 2002, *MNRAS*, 334, 589

Wyatt, M. C., Dermott, S. F., Telesco, C. M., et al. 1999, *ApJ*, 527, 918

Wyatt, M. C., Panić, O., Kennedy, G. M., & Matrà, L. 2015, *AP&SS*, 357, 103